ALGORITHM THEORETICAL BASIS DOCUMENT (ATBD) FOR THE THE AMSR SEA ICE ALGORITHM

Donald J. Cavalieri
Laboratory for Hydrospheric Processes
NASA Goddard Space Flight Center
Greenbelt, Maryland 20771
Phone (301) 286–2444, Fax (301) 286–0240
email: don@cavalieri.gsfc.nasa.gov

and

Josefino C. Comiso
Laboratory for Hydrospheric Processes
NASA Goddard Space Flight Center
Greenbelt, Maryland 20771
Phone (301) 286–9135, Fax (301) 286–0240
email: comiso@joey.gsfc.nasa.gov

January 15, 1997

Table of Contents

1.0 INTRODUCTION

Sea ice is a vital component of the global climate system because of its high albedo, its role in limiting the exchange of heat, mass, and momentum between the ocean and atmosphere, and its influence on oceanic water mass properties. Current interest in long–term sea ice changes results from the observed increase of CO_2 in the atmosphere. Because of expected feedback effects, the anticipated global warming from an increase in CO_2 was postulated to be amplified in the polar regions (Budyko (1966). Some coupled ocean–atmosphere model results (e.g., Manabe and Stoufer, 1994) suggest that a doubling of CO_2 would lead to a significant thinning and reduction in the extent of the Arctic sea ice cover, especially during the summer periods.

Sea ice with its snow cover very effectively insulates the ocean from the atmosphere, because its heat conductivity is relatively low. For example, in winter, the heat flux in an open lead exceeds by two orders of magnitude that through an adjacent thick ice cover (Badgley, 1966; Maykut, 1978). Sea ice also influences the oceanic and atmospheric circulations. During ice growth, the cold saline dense water produced induces convection that tends to deepen the mixed layer. Deep ocean convection also associated with this densification contributes to driving the thermohaline circulation of the world's ocean (Bryan et al., 1975). Furthermore, much of the world's deep and bottom water is believed to be formed at polar latitudes (Stommel, 1962; Gordon, 1978; Killworth, 1983).

The effect of sea ice on the atmospheric circulation results from its high albedo,which ranges from about 80% (Grenfell, 1983) to 98% (Vowinckel and Orvig, 1970), relative to that of the open ocean (10% to 15%), and the sharp thermal and surface stress boundaries associated with the edge of the ice pack. The abrupt change in energy exchange that takes place at the ice margin can, under the appropriate atmospheric conditions, gives rise to violent weather systems known as polar lows (Carleton, 1985; Businger and Reed, 1989; Gloersen et al., 1989). A more recent study making use of an atmospheric general circulation model suggests an association between heavy and light ice years and larger scale atmospheric circulation changes (Honda et al., 1996).

A long–term, large–scale characterization of the global sea ice cover is needed for sea ice trend studies and for climate model validation studies. The most consistent source of such data continues to be satellite passive microwave sensors (Zwally et al., 1983; Parkinson et al., 1987; Gloersen et al., 1992). Visible and infrared satellite data (e.g., AVHRR) can be used for large scale and mesoscale studies but coverage is limited by persistent cloud cover. Detailed characterization of sea ice under all weather conditions has recently been provided by the ERS–1 and JERS–1 synthetic aperture radar (SAR) data, but only a small fraction of the entire ice cover can be monitored at a time because of operational and data acquisition constraints and a narrow swath width (100 km). Radarsat data with its wider swath (500 km) is an improvement but adequate temporal resolution is still lacking. Such data are nonetheless useful for regional studies and may provide information to improve the interpretation of passive microwave data.

The principal quantitative measure of the global sea ice cover is sea ice concentration. It is this parameter that continues to be produced routinely from satellite passive microwave systems for both global change research and operational requirements. In addition to sea ice concentration, other sea ice parameters that are important to the accurate determination of surface energy fluxes are snow depth on sea ice and the physical temperature of the ice. The surface heat flux through sea ice critically depends on the depth of snow which is a very effective

insulator. While snow fall is an externally prescribed quantity in sea ice models, there is nevertheless a need for information on the distribution of snow depth on sea ice to permit modelers to determine whether observed biases in simulated sea ice (e.g. thickness) can be attributed to biases in the climatologically prescribed snowfall (Preller et al., 1992).

Another major source of uncertainty in energy balance calculations is ice surface temperature. Direct measurement of ice surface temperature would be particularly valuable for ice prediction models (Preller et al., 1992). While AVHRR ice surface temperature algorithms have been developed (e.g., Comiso, 1983; Schluessel and Grassl, 1990), spatial and temporal coverage is limited by the presence of clouds as noted earlier. For the seasonal sea ice cover, the sea ice temperature measured by microwave radiometers represents the snow/ice interface temperature and when combined with the snow depth measurement would considerably reduce current uncertainties in polar energy budgets.

The AMSR system as configured will be a significant improvement over previous and current passive microwave systems. The most obvious improvements are its finer spatial resolution and its wider spectral range. This capability will allow an improved determination of our three standard products: total sea ice concentration, snow depth on sea ice, and sea ice temperature. The AMSR sea ice algorithm presented below will provide daily maps of sea ice concentration, sea ice temperature, and snow depth.

2.0 OVERVIEW AND BACKGROUND INFORMATION

2.1 Experimental Objectives

The prime objectives of this document are (a) to describe and justify the standard and special sea ice products that will be derived from AMSR; (b) to provide the theoretical basis of the algorithms that will be used to generate these standard and special products; and (c) to assess the accuracy of these products. The standard products are those sea ice products which are deemed essential to meet the overall objectives of NASA's MTPE. The special products are of interest to the research community, but not sufficiently tested and validated to warrant their classification as standard products. The standard and special products are listed in Table 1. Accuracies will be estimated with the aid of a comprehensive validation program. This program entails the comparison of the AMSR ice products with corresponding products derived from visible and infrared satellite imagery, from spaceborne SAR, and from high−resolution passive microwave imagery from aircraft underflights.

TABLE 1. AMSR Standard and Special Sea Ice Products.

_____

Standard Products: Sea Ice Concentration

Sea Ice Temperature

Snow Depth on Sea Ice

 Special Products: Sea Ice Motion

Sea Ice Type

Sea Ice Surface Class

_____

2.2 Historical Perspective

The first global view of sea ice was achieved in the early 1960s with the launch of earth–viewing satellite sensors such as those aboard the Nimbus, Tiros, and Earth Resources and Technology (ERTS, later, Landsat) satellites. Because these sensors operated in the visible and infrared bands of the electromagnetic spectrum, they were limited to cloud–free and well–illuminated regions only, making them incapable of providing the synoptic observations needed for processes and climate studies. Microwave sensors, not limited by weather conditions or light levels, are particularly well suited for monitoring sea ice, because of the strong contrast in thermal microwave emission between areas of ice–free ocean and ice–covered waters.

The first passive microwave sensor used extensively for studying the global distribution of sea ice was the Electrically Scanning Microwave Radiometer (ESMR) on board the NASA Nimbus 5 satellite (Gloersen et al., 1974; Zwally et al., 1983). The single channel ESMR, operating at 19.35 GHz, provided daily coverage of the polar regions and allowed for the first time synoptic observations of sea ice concentration needed for undertaking a detailed study of global sea ice variability. The ESMR sea ice algorithm was based on a linear relationship between the radiometric brightness temperatures of ice–free water and consolidated sea ice. Temperature variability effects were reduced using climatological data. At the ESMR frequency the contrast between ice and water is ~100 K. Although the estimated accuracy was only 15% (Comiso and Zwally, 1982), these data were used successfully to document sea ice changes in both hemispheres (Zwally et al.,1983; Parkinson et al., 1987).

The Scanning Multichannel Microwave Radiometer (SMMR) was launched on the SeaSat satellite in July 1978 and on the Nimbus–7 satellite in October 1978 (Gloersen et al. 1992). With its multichannel capability, SMMR provided more information about the ice cover than ESMR. Multichannel SMMR algorithms extended the calculation of ice concentration to include the discrimination of two ice types, first–year and multiyear in the Arctic (Svendsen et al., 1983; Cavalieri et al., 1984; Swift et al., 1985). A multichannel SMMR algorithm to obtain sea ice concentration only was also developed (Comiso and Sullivan, 1986; Comiso, 1986). The various algorithms take advantage of two or more channels to reduce errors associated with physical temperature variability, emissivity anomalies, and weather effects.

In 1987, the first in a new series of passive microwave radiometers was launched as part of the Defense Meteorological Satellite Program (DMSP). This sensor, called the Special Sensor Microwave Imager (SSMI), operates at frequencies ranging from 19.4 GHz to 85.5 GHz. The SSMI measures both horizontally and vertically polarized components at all frequencies except at 22.2 GHz for which only a vertically polarized component is obtained. Using these data, several new algorithm improvements have been made (e.g., Cavalieri, 1994; Comiso, 1995).

The AMSR sensor, which will have a wider range of frequencies and an improved spatial resolution, should provide the basis for improving the current suite of sea ice algorithms and for developing new hybrid algorithms.

2.3 AMSR Instrument Characteristics

The EOS PM–1 AMSR is a twelve channel, six frequency total power passive microwave radiometer system. It measures vertically and horizontally polarized radiances at 6.925, 10.65, 18.7, 23.8, 36.5, and 89.0 GHz.

The instrument, modified from the design used for the ADEOS–II AMSR, consists of an offset parabolic reflector 1.6 m in diameter, fed by an array of six feedhorns. The AMSR rotates continuously at 40 rpm about an axis parallel to the local spacecraft vertical. At an altitude of 705 km, it measures the upwelling scene brightness temperatures over an angular sector of $\pm$ 61° about the sub–satellite track, resulting in a swath width of 1445 km. During a period of 1.5 seconds the spacecraft sub–satellite point travels 10 km. Even though the instantaneous field–of–view (IFOV) for each channel is different, active scene measurements are recorded at equal intervals of 10 km (5 km for the 89 GHz channels) along the scan. The half–cone angle at which the reflector is fixed is 47.4^O which results in an Earth incidence angle of 55.0^O. Table 2 lists the pertinent performance characteristics

Table 2. EOS PM–1 AMSR SENSOR PERFORMANCE CHARACTERISTICS

CHARACTERISTICS	CENTER FREQUENCIES (GHz)					
	6.9	10.7	18.7	23.8	36.5	89.0
BANDWIDTH (MHz)	350	100	200	400	1000	3000
SENSITIVITY (K)		0.3	0.6	0.6	0.6	0.6
1.1						
IFOV (km x km)	76x44	49x28	28x16	31x18	14x8	6x4
SAMPLING RATE (km x km)	10x10	10x10	10x10	10x10	10x10	5x5
INTEGRATION TIME (ms)	2.6	2.6	2.6	2.6	2.6	1.3
MAIN BEAM EFFICIENCY (%)	95.3	95.0	96.3	96.4	95.3	96.0
BEAMWIDTH (degrees)	2.2	1.4	0.8	0.9	0.4	0.18

The radiometer calibration error budget, exclusive of antenna pattern correction effects, is composed of three major contributors: warm load reference error, cold load reference error, radiometer electronics nonlinearities and errors. An estimate of the warm load reference error is ~0.5 K, based on the RSS of the various components. The error in the cold reference measurement is mainly produced by the error in coupling between the cold sky reflector and the feedhorn. This is estimated to be ~0.5 K. The radiometer electronics nonlinearity results in an error that can be estimated during the thermal vacuum calibration testing (on SSMI this error was ~0.4 K). A source of error in the receiver electronics is the gain drift resulting from temperature variations over one orbit. This error depends on the design of the receiver and overall design of the sensor. The gain drift can be as much as ~0.24 K for a temperature variation of less than 10 K over one orbit. Accounting for all errors, the total sensor bias error is 0.66 K at 100 K and changes with temperature to 0.68 K at 250 K.

3.0 ALGORITHM DESCRIPTION AND THEORETICAL BASIS

The proposed multichannel AMSR sea ice algorithm builds on our experience with the Nimbus 7 SMMR and the DMSP SSMI sensors and on the expected configuration of the AMSR sensor itself. The functional form of the AMSR sea ice concentration algorithm combines

aspects of the SSMI version of the NASA Team sea ice algorithm (Cavalieri et al., 1992) and the Bootstrap algorithm (Comiso, 1995). In some areas of the Arctic, the SSMI thin ice algorithm (Cavalieri, 1994) will be used to improve the determination of ice concentration. The initial algorithm output will be tested and checked for internal consistency and for consistency with ice parameters derived from other sensors. The sea ice temperature algorithm is a modified version of that used in Gloersen et al.(1992) and is part of the temperature independent Bootstrap algorithm, whereas the snow depth algorithm is based on more recent work (Markus and Cavalieri, 1997).

A block diagram illustrating the components of the algorithm for computing the standard products of sea ice concentration, sea ice temperature, and   snow cover on sea ice is shown in Figure 1. The plan for obtaining sea ice concentration is illustrated in Figure 1a. Initially, sea ice concentrations will be derived using both the NASA Team algorithm and a temperature independent form of the Bootstrap algorithm currently under development (Figure 1b).   A difference map of the results is then generated to determine areas A of ice concentration differences exceeding about 5%. The next step is to correct the NASA Team ice concentrations for those areas A that satisfy a yet to be determined threshold using the temperature independent Bootstrap algorithm, and in limited areas of the Arctic, using the thin ice algorithm (Cavalieri, 1994). A similar threshold approach was used successfully in the application of the thin ice algorithm to Arctic seasonal sea ice zones (SSIZs), where the threshold was defined in terms of the NASA Team algorithm variables PR and GR. A quantitative comparison of the NASA Team and Bootstrap algorithm results is presented in Comiso et al. (1997). The plan is to generate validated hybrid concentrations that take advantage of the strengths of each of the two algorithms.

Sea ice temperatures will be derived from the surface ice temperatures that are inferred from the temperature corrected Bootstrap algorithm. A mixing formalism and the final ice concentration value are used for each data element to separate contributions from the open water (Figure 1b). The ice temperature product is thus basically the physical temperature of the snow/ice interface in seasonal ice regions and the weighted–average temperature of the freeboard portion of the ice in the Arctic multiyear ice regions. Snow depth over sea ice will be derived from the enhanced ice concentrations and AMSR brightness temperatures. As indicated in Figure 1c, snow depths will be calculated for the entire Antarctic sea ice pack and for the Arctic only where the concentration of multiyear ice is less than 20%. The rationale for the Arctic limitation is discussed in section 3.1.2.

3.1 Standard Products

The principal sea ice parameter derived from AMSR radiances is sea ice concentration. It is this product that enables the spatial characterization of the sea ice cover and the calculation of sea ice extent and area that are used in long–term trend analyses and processes studies. The calculation of the two other standard products, ice temperature and snow depth on sea ice, also requires sea ice concentration as input. All three products are important to the calculation of the surface heat exchange.

3.1.1 Sea Ice Concentration

The two basic assumptions made in the development of the sea ice concentration algorithm are (1) that the received radiation by the satellite sensor comes from three dominant polar ocean surface types: two types of sea ice (A and B), and ice–free (open) water (W), and (2) that the
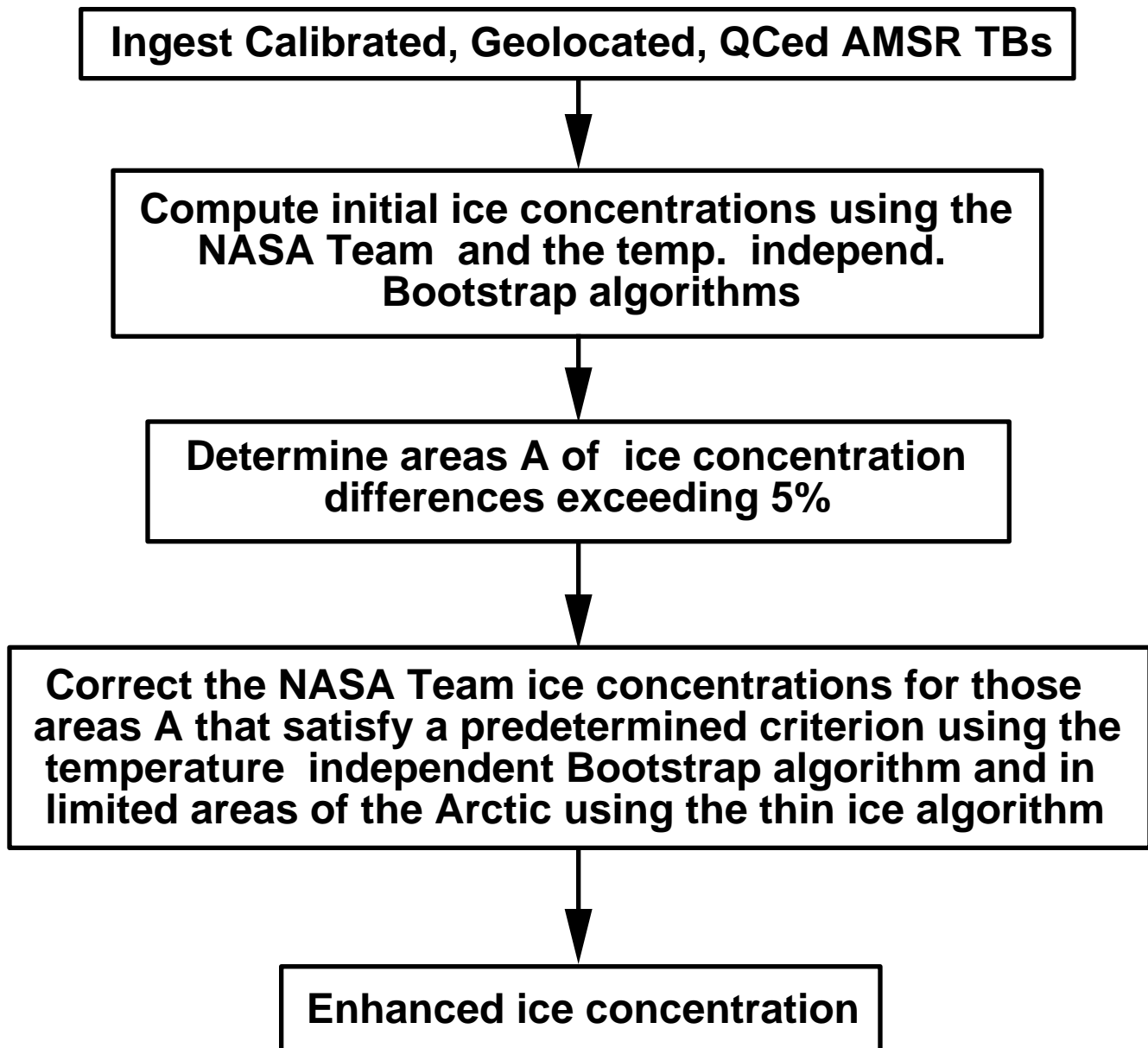
AMSR SEA ICE CONCENTRATION ALGORITHM

Ingest Calibrated, Geolocated, QCed AMSR TBs

Compute initial ice concentrations using the NASA Team and the temp. independ. Bootstrap algorithms

Determine areas A of ice concentration differences exceeding 5%

Correct the NASA Team ice concentrations for those areas A that satisfy a predetermined criterion using the temperature independent Bootstrap algorithm and in limited areas of the Arctic using the thin ice algorithm

Enhanced ice concentration

Figure 1a.   Flow chart for the AMSR sea ice concentration algorithm.

TEMPERATURE CORRECTED BOOTSTRAP ALGORITHM

Use Bootstrap Results for Initial Ice Concentration

↓

Calculate Effective Emissivity Using a Mixing Formulation

↓

Calculate Physical Temperature of Emitting Layer

↓

Calculate Effective Emissivity at 18 GHz and 37 GHz for V−pol

↓

Recalculate Ice Concentration Using New Effective Emissivities

↓

C−Ci>3% — **Yes** →

No ↓

Calculate Physical Ice Temperature

↓

Store Final Ice Concentrations and Ice Temperatures

Figure 1b. Flow chart for the Temperature Corrected Bootstrap Algorithm and physical ice temperature.
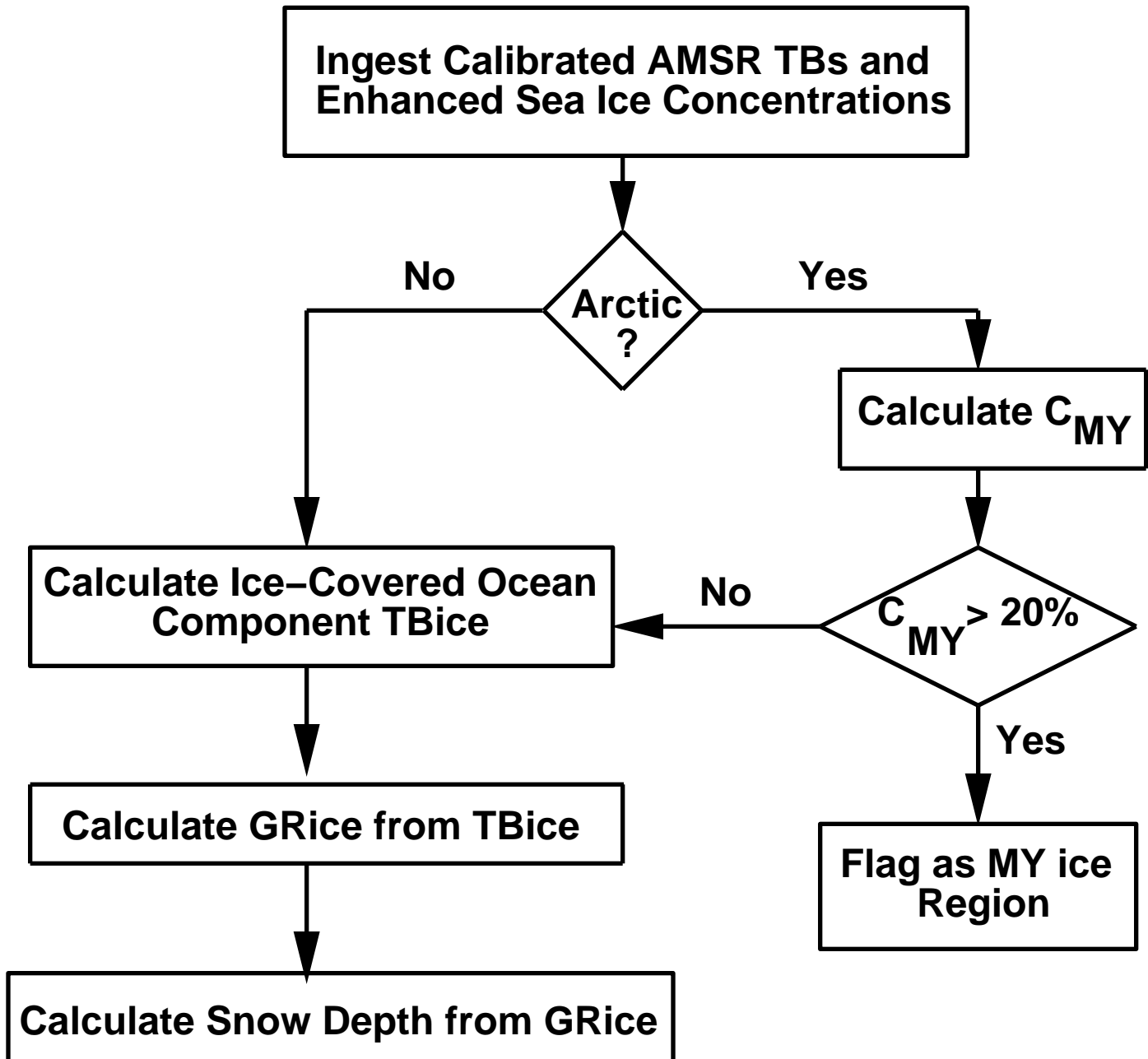
AMSR SNOW DEPTH
ON SEA ICE ALGORITHM

```
┌─────────────────────────────────────┐
│  Ingest Calibrated AMSR TBs and     │
│  Enhanced Sea Ice Concentrations    │
└─────────────────────────────────────┘
                  │
                  ▼
No          ◇ Arctic ? ◇          Yes
  │                                  │
  │                                  ▼
  │                        ┌──────────────────┐
  │                        │  Calculate $C_{MY}$ │
  │                        └──────────────────┘
  │                                  │
  ▼                                  ▼
┌─────────────────────────┐   No  ◇ $C_{MY} > 20\%$ ◇
│ Calculate Ice–Covered   │ ◄─────
│ Ocean Component TBice    │                 │ Yes
└─────────────────────────┘                 ▼
       │                        ┌──────────────────┐
       ▼                        │  Flag as MY ice  │
┌─────────────────────────┐     │     Region       │
│ Calculate GRice from    │     └──────────────────┘
│ TBice                   │
└─────────────────────────┘
       │
       ▼
┌─────────────────────────────┐
│ Calculate Snow Depth from   │
│ GRice                       │
└─────────────────────────────┘
```

Figure 1c. Flow chart for the AMSR snow–depth on sea ice algorithm.

atmospheric contribution is approximately constant. The selection of algorithm coefficients (tie–points) is based on observed brightness temperatures which include an atmospheric component. Later, weather filters are employed to eliminate spurious sea ice concentrations over open ocean resulting from a varying atmospheric emission.

Using a linear mixing formulation, the received radiation expressed as a brightness temperature is given by

$$T_B = T_{BW}C_W + T_{BIA}C_{IA} + T_{BIB}C_{IB} \tag{1}$$

where T_{BW}, T_{BIA}, and T_{BIB} are the brightness temperatures of ice–free ocean, ice–type A, and ice–type B, respectively. C_W, C_{IA}, and C_{IB} are the corresponding fractions of each of the three ocean surface components within the field–of–view of the instrument and add to unity. Equation (1) is the fundamental equation that is used to develop the NASA Team algorithm. In the northern hemisphere, the two dominant ice types are first–year (FY) ice and multiyear (MY) ice, whereas in the southern hemisphere the two ice types are simply labeled A and B, because of ambiguities in distinguishing between seasonal and perennial sea ice in the Antarctic. The temperature corrected Bootstrap algorithm also uses equation (1), but assumes only two types of surfaces, namely ice and water.

3.1.1.1 NASA Team Formulation

The physical basis for distinguishing among the three polar ocean components is best described by considering the brightness temperature spectra of Arctic polar ocean surfaces shown in Figure 2. Examination of this figure illustrates two important characteristics. First, the difference between the vertically and horizontally polarized radiances is small for either ice type (FY or MY) in comparison to that for the ocean. Second, the discrimination between ice types increases with decreasing wavelength (increasing frequency). In particular, discrimination between FY and MY ice is greater at 0.8 cm (37 GHz) than it is at 1.7 cm (18 GHz). These characteristics are parameterized in terms of two independent variables, the polarization (PR) and the spectral gradient ratio (GR), defined by:

$$PR(19) = (T_B(19V) - T_B(19H))/(T_B(19V) + T_B(19H)) \tag{2}$$

$$GR(37V/19V) = (T_B(37V) - T_B(19V))/(T_B(37V) + T_B(19V)) \tag{3}$$

These variables have been shown to have the same functional form as principal components and differ only in that these variables are normalized (Rothrock et al., 1988). An advantage of using normalized principal components is that they are less susceptible to geophysical crosstalk. Another advantage of these variables is that they are largely independent of ice temperature variations, which eliminates the problem of estimating ice temperature variability both temporally (e.g., day–to–day and seasonal) and spatially (e.g., temperature gradients across the Arctic basin).

Equation (1) is used with the definitions of PR and GR to solve for ice–type A and ice–type B concentrations. The expressions for CIA and CIB are:

$$C_{IA} = [a_0 + a_1 PR + a_2 GR + a_3(PR)(GR)]/D \tag{4}$$

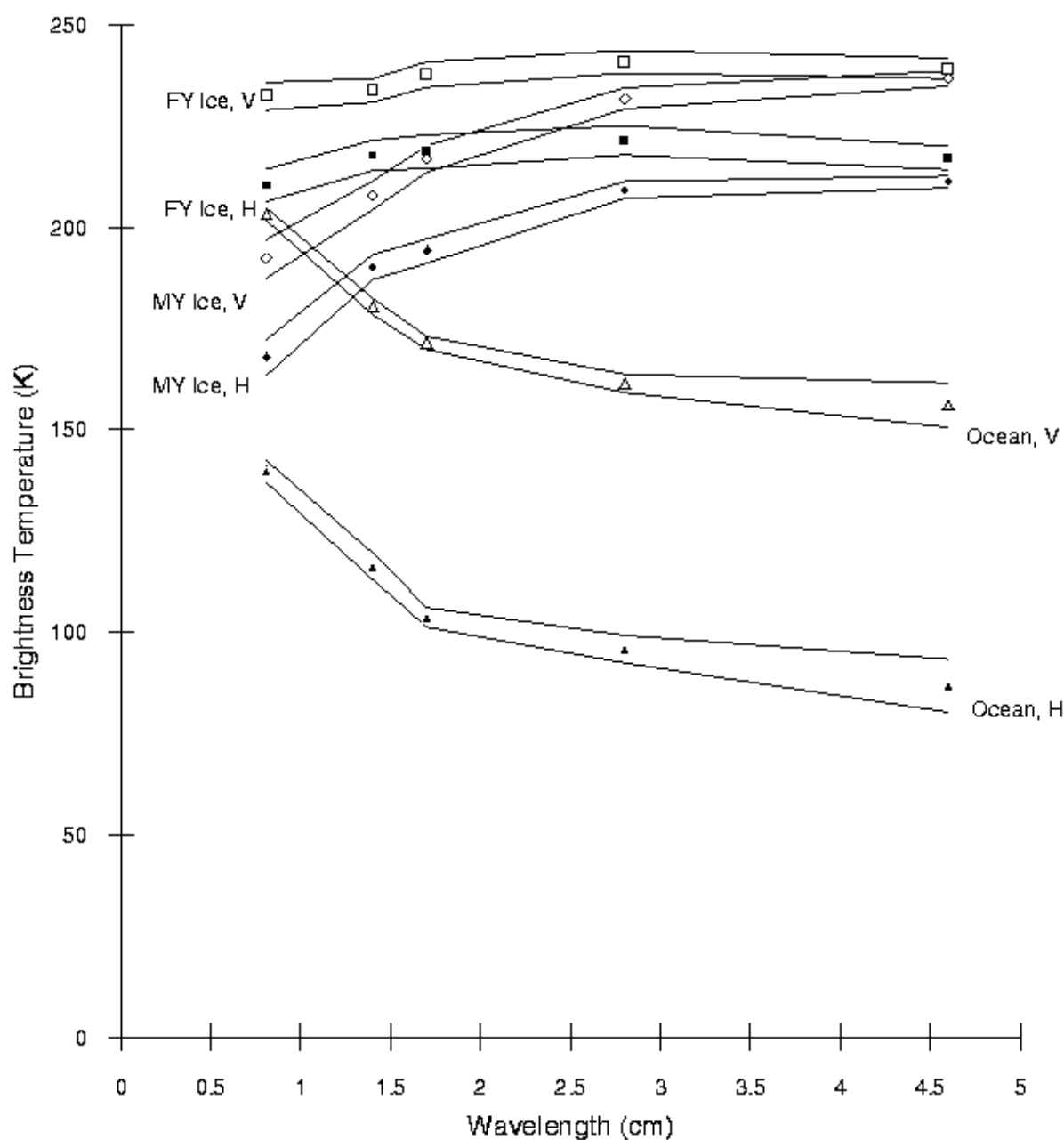$$C_{IB} = [b_0 + b_1 PR + b_2 GR + b_3(PR)(GR)]/D \tag{5}$$

Figure 2. Microwave spectra of first–year and multiyear sea ice, and ice–free ocean for horizontal and vertical polarizations. The plotted values represent the mean ±1 standard deviation (reprinted from Gloersen et al., 1992).

where, $D = c_o + c_1 PR + c_2 GR + c_3 (PR)(GR)$ (6)

The total ice concentration C_I is the sum of the two ice–type concentrations

$$C_I = C_{IA} + C_{IB} \qquad\qquad\qquad (7)$$

The coefficients a_i, b_i, and c_i ($i = 0, 3$) are functions of a set of nine T_Bs. These T_Bs, referred to as algorithm tie–points, are observed radiances over areas of known ice–free ocean, and ice types during winter for each of the three AMSR channels.
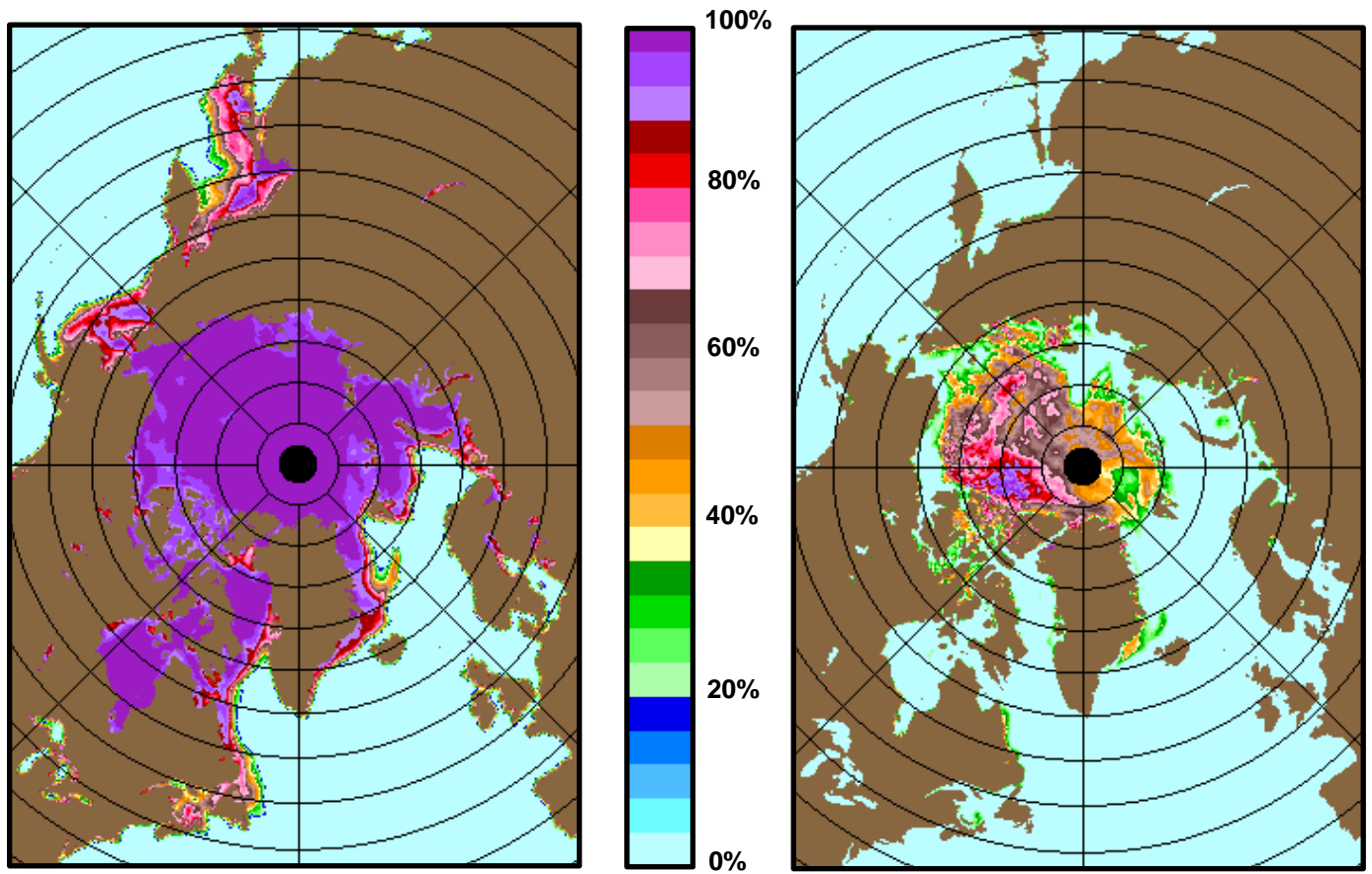
Figure 3.   Arctic monthly mean maps of total and multiyear sea ice concentration derived from DMSP SSMI radiances for March 1988.

Examples of retrieved total and multiyear sea ice concentrations for the Arctic are illustrated in Figure 3.

3.1.1.2 Temperature Corrected Bootstrap Formulation

The ice concentration, C_I, corresponding to an observed brightness temperature, T_B, can be derived from the mixing formulation with all ice types combined and is given by:

$$C = (T_B - T_O)/(T_I - T_O) \qquad (8)$$

where T_O, and T_I are reference brightness temperatures of open water and sea ice, respectively. T_O, T_I, and T_B all include contributions from the intervening atmosphere, as described in Zwally et al. (1983). T_I varies spatially because of spatial changes in the emissivity and temperature of the ice, while T_O is approximately constant for open water surfaces within the ice pack.

In the Bootstrap formulation (Comiso, 1995) T_I and T_O are determined with the aid of two sets of channels: (a) 19 GHz and 37 GHz radiances both vertically polarized (called V1937); and (b) vertically and horizontally polarized 37 GHz radiances (called HV37). Scatter plots using each set of channels (Figure 4a and 4b) indicate that data points aboutAD are highly correlated and correspond to consolidated ice regions. This has been confirmed by ship data as well as aircraft data (e.g., Figure 11 of Comiso (1995)). For a given data point B, T_I is inferred, and ice concentration is determined from equation (8), or an equivalent formulation as described in Comiso (1995).

The use of V1937 is desirable because it uses solely the vertical channels which are less affected by layering and inhomogenuities in the ice (Matzler, 1984; Grenfell et al., 1994) than are the horizontal channels. This set has been found to be most suitable in the Antarctic Region (Comiso et al., 1984; Comiso and Sullivan, 1986) where snow cover is known to have a very complex texture (Massom et al., 1996; Worby and Massom 1995). However, the V1937 set is more sensitive to fluctuations in ice temperature than the HV37 set (Comiso, 1995). Although spatial variations in surface ice temperature were observed in the Weddell Sea to be small (standard deviation of about 2K), other studies show larger variability (Sturm et al., 1996) and there are also regions where the surface may be considerably colder than average (e.g., thick ice with little or no snow cover in the inner zone).

To correct for temperature effects on the V1937 set, we make use of snow/ice interface temperatures that can be derived from the 6 GHz V−pol. channel. The effective emissivity of the surface within each data element can be obtained from:

$$e_B = e_I C_I + e_O(1 - C_I) \qquad (9)$$

where C_I is obtained from equation 8, while e_I and e_0 are emissivities of ice and water, respectively, which can be derived from the data and assumed constant. Unlike equation (8), equation (9) is not exact but a sensitivity study indicates that the error is very small (<1%) and is highest when the concentration is 50%. The physical temperature of each data element is then given by

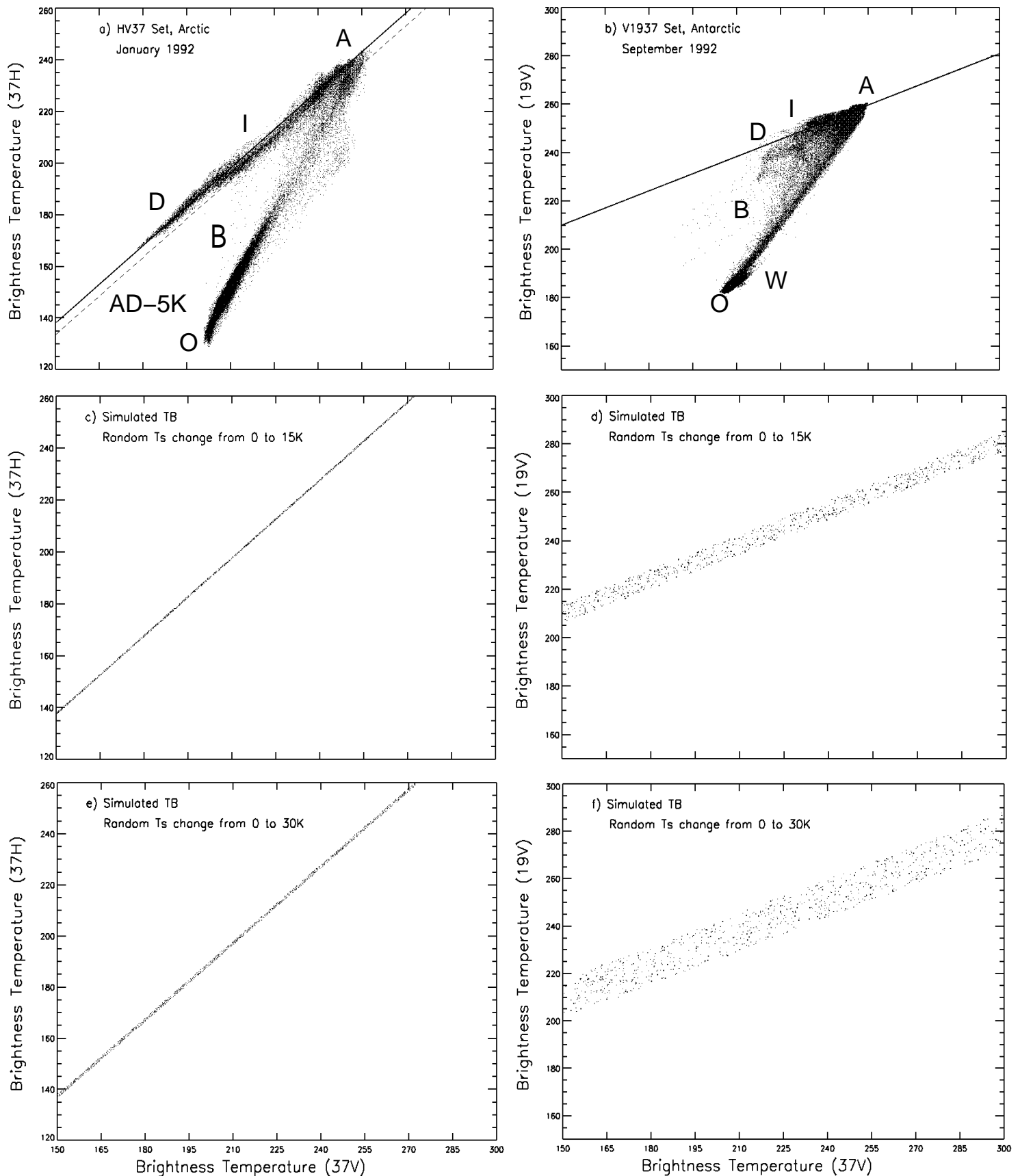$$T_p = T_B(6V)/e_B(6V) \qquad (10)$$

Figure 4.   (a) Scatter plot of 37H versus 37V SSMI monthly January 1992 data for the entire Arctic region; (b) scatter plot of 19V versus 37V SSMI monthly September 1992 dat for the entire Antarctic region; (c) simulated 37H versus 37V brightness temperatures for changes in surface ice temperatures randomly selected from 0 to 15K; (d)simulated 19V versus 37V brightness temperatures for changes in surface ice temperatures randomly selected from 0 to 15K; (e) simulated 37H versus 37V brightness temperatures for changes in surface ice temperatures randomly selected from 0 to 30K; (f) simulated 19V versus 37V brightness temperatures for changes in surface ice temperatures randomly selected from 0 to 30K.

15

where $T_B(6V)$ is the observed brightness temperature of the surface at 6 GHz (vertical polarization). The emissivity of the surface at 19 and 37 GHz can then be derived from

$$e(19V) = T_B(19V)/T_p(19V) \tag{11}$$

and

$$e(37V) = T_B(37V)/T_p(37V) \tag{12}$$

with the assumption that $T_p(19V)$ and $T_p(37V)$ are equivalent to $T_p(6V)$. The ice concentration can be inferred from these derived emissivities using a formulation similar to that described in Comiso (1995). The use of emissivity instead of brightness temperature is justified by the matching of reference data points of both consolidated ice (100% IC) and open water (0% IC). As in Comiso (1995), the tie points for the emissivity of 100% ice can be calculated from

$$e_{1I} = (e_{1A}-e_{1O}-e_{2A}S_{AD}+e_{2O}S_{OB})S_{OB}/(S_{OB}-S_{AD})+ e_{1O} - S_{OB}e_{2O} \tag{13}$$

$$e_{2I} = (e_{1A}-e_{1O}-e_{2A}S_{AD}+e_{2O}S_{OB})/(S_{OB}-S_{AD}) \tag{14}$$

where S_{AD} and S_{OB} are slopes of the lines AD and OB, respectively, (e_{1A}, e_{2A}) represents any point along the line AD, and (e_{1O}, e_{2O}) represents the open water reference brightness temperature. The ice concentration for any data point B can be derived from the ratio of the distances OB and OI given by the equation (see Figure 4):

$$C = [\{(e_{1B}-e_{1O})^2+(e_{2B}-e_{2O})^2\}/\{(e_{2I}-e_{2O})^2 + (e_{1I}-e_{1O})^2\}]^{1/2} \tag{15}$$

In the formulation, it is convenient to choose $e_{2A}=0$ at point A along AD with e_{1A} the resulting offset. Additional details, including the determination of the line AD and the point O, are given in Comiso (1995). Since the initial calculation of the emissivity at 6 GHz make use of ice concentration that has not been temperature corrected, the emissivity is recalculated using the more accurate result from equation (15) and using the same procedure, the ice concentration is recalculated. The final value will be the estimate for the temperature corrected Bootstrap ice concentration. Also, the final value of T_p is the estimate of the physical temperature within the data element. (Figure 1b) The advantage of using emissivities instead of brightness temperature is illustrated in Figure 5. The data points along AD in Figure 5a are the points that are in the inner zone and have high ice concentrations as indicated earlier. When the same set of data are plotted using emissivities, these points became more compact and better correlated as shown in Figure 5b. The use of emissivity instead of brightness temperature thus improves the determination of the ice concentration since the standard deviation along the consolidated ice line (AD) is significantly better (a 33% improvement) when the former is used.

Ice concentration maps using the Team algorithm and this procedure on SMMR data (September 15, 1979) when a 6 GHz channel was available are shown in Figure 6a and 6b, respectively. The difference between the two is shown in Figure 6c while the surface temperature for each pixel as derived using the 6 GHz data is shown in Figure 6d. The difference map presented in Figure 6c shows the typical magnitude of the discrepancies between the two algorithms and maps such as this will be used as guidelines for the implementation of the threshold technique for the hybrid algorithm. The lack of validation data set makes it difficult to assess accuracies. However, winter Landsat data were available on September 18, 1988.
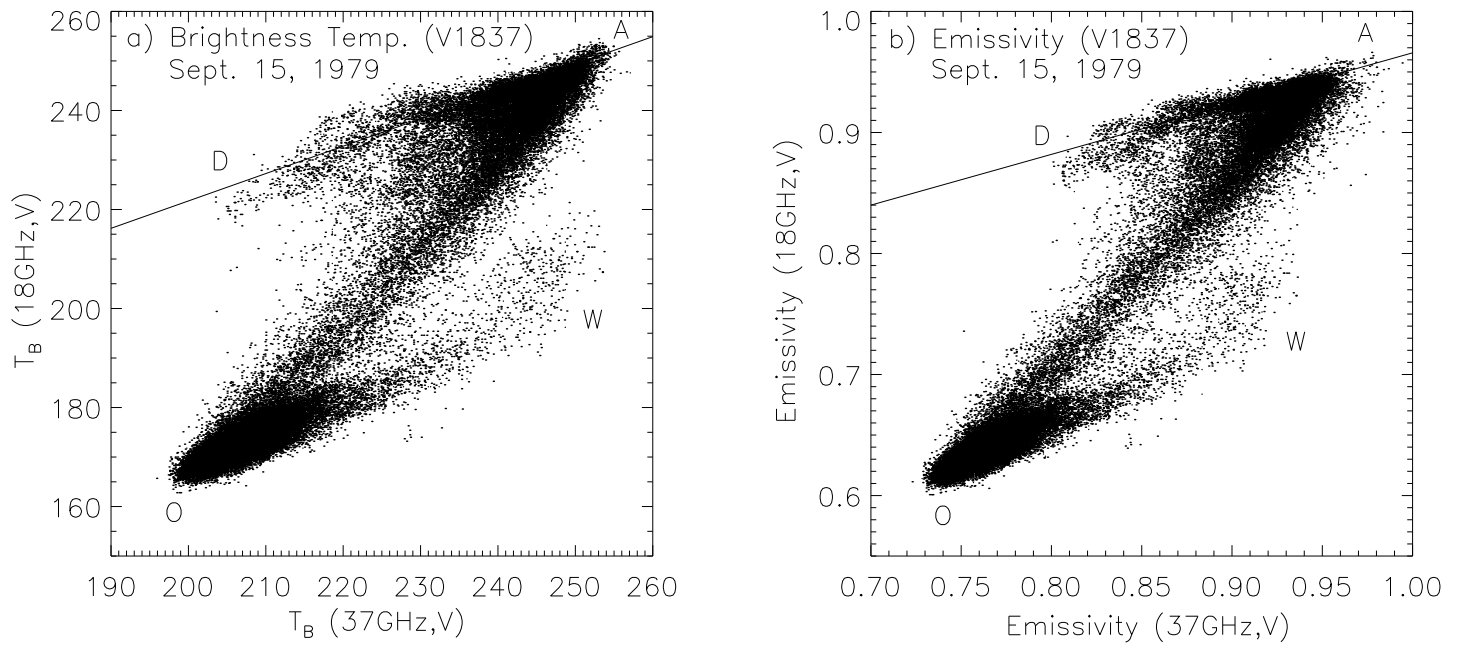
Figure 5. Scatter plot of vertically polarized 18 GHz versus 37 GHz SSMI data using (a) brightness temperatures, and (b) emissivities, inferred with the use of 6 GHz data.

For this day, only SSMI data are available and there are no 6 GHz data to be used for correcting the Bootstrap Algorithm. However, the effect of spatially varying temperature is simulated with the use of a climatological average of ice temperature (from Gloersen et al., 1992) as was done in Zwally et al. (1983). The emissivity is calculated in a similar manner as indicated earlier and the ice concentration maps before and after the temperature correction is used are shown in Figures 7a and 7b, respectively. The difference between the two is shown in Figure 7c and the Landsat image at the location of the box in Figure 7a and 7b, is shown in Figure 7d. The ice concentration from Landsat data show agreement with that from the temperature corrected Bootstrap technique within 2%. The negative values in the coastline areas correspond to colder regions in the temperature maps and indicates where the enhanced Bootstrap technique can show substantial improvements. More extensive validation of the latter with Landsat images will be implemented.

3.1.1.3 Correction for Thin Ice in Arctic Seasonal Sea Ice Zones

The NASA Team algorithm is capable of distinguishing among three Arctic Ocean surface types: open water (OW), first-year (FY) ice, and multiyear (MY) ice. The problem of not being able to discriminate among new, young and first-year ice leads to a negative bias in the retrieved sea ice concentration (Cavalieri, 1994). To help understand how the algorithm misinterprets the
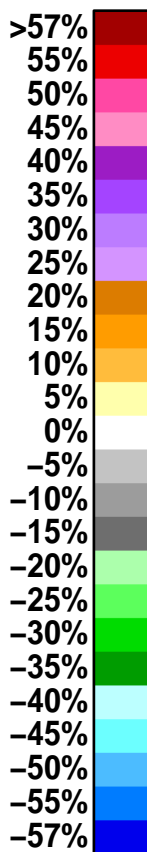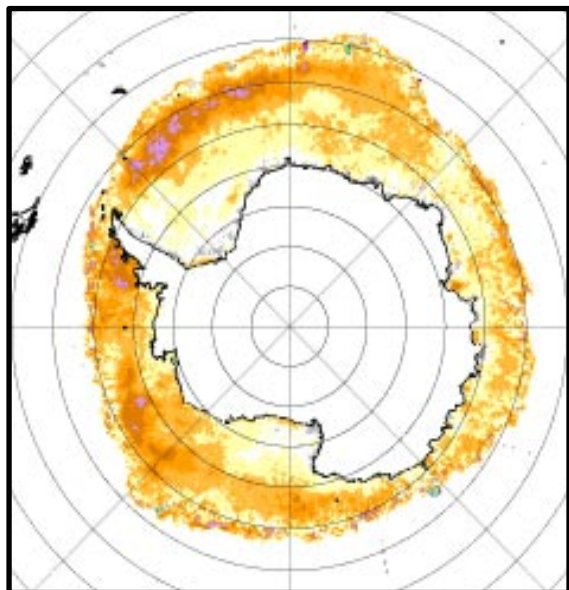
17

(a) TEAM Algorithm
September 15, 1979
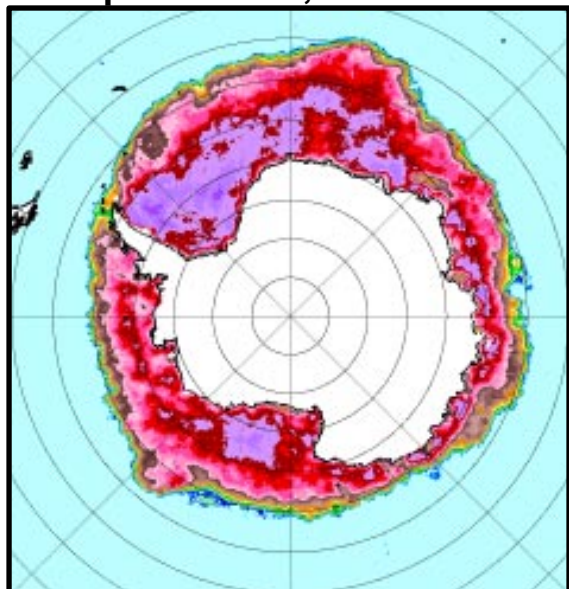
(b) Revised Bootstrap Algorithm
September 15, 1979
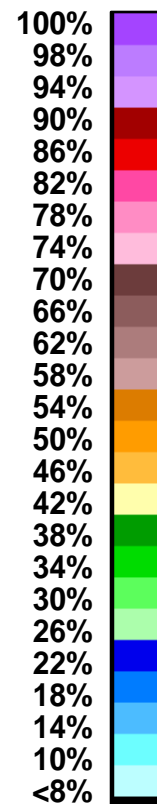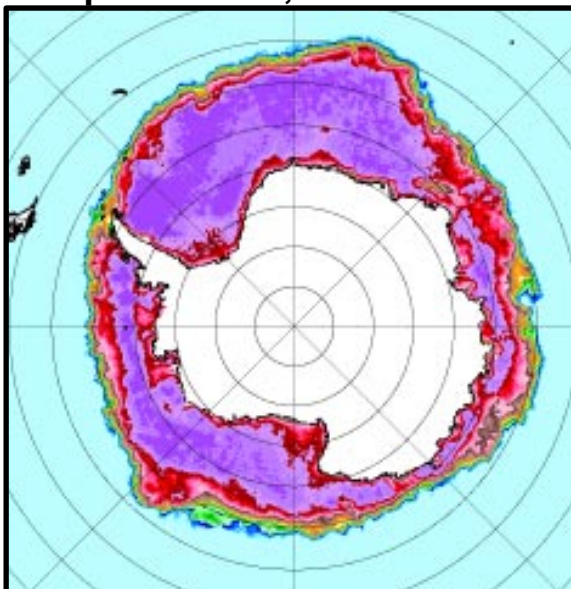
(c) Difference [(b) − (a)]
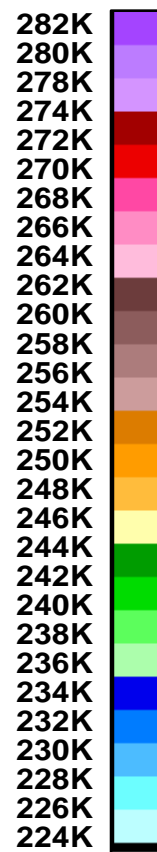
(d) Ts (6 GHz)
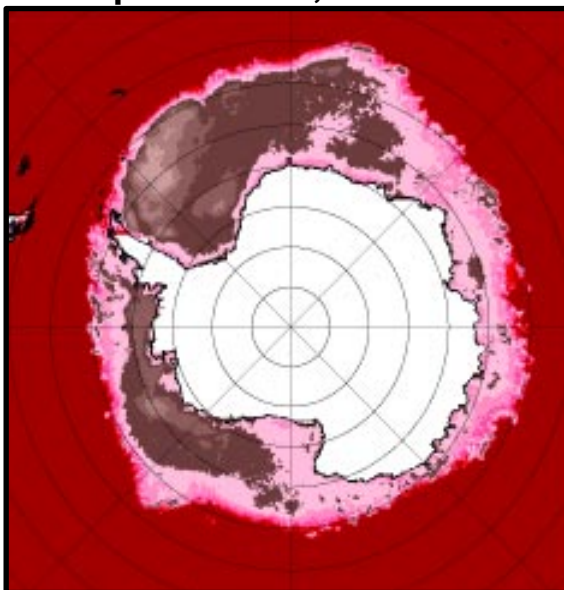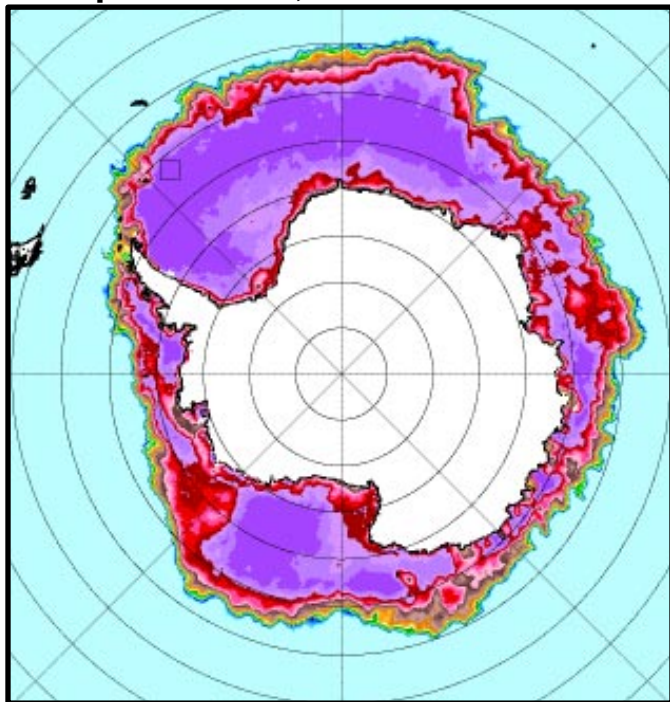September 15, 1979

Figure 6.   (a) Ice concentration map on September 15, 1979 using the PR−GR algorithm; and (b) Ice concentration map on September 15, 1979 uisng the temperature corrected bootstrap algorithm; (c) difference between (a) and (b); and (d) surface ice temperature map from the 6 GHz channel on September 15, 1979 used in (b).

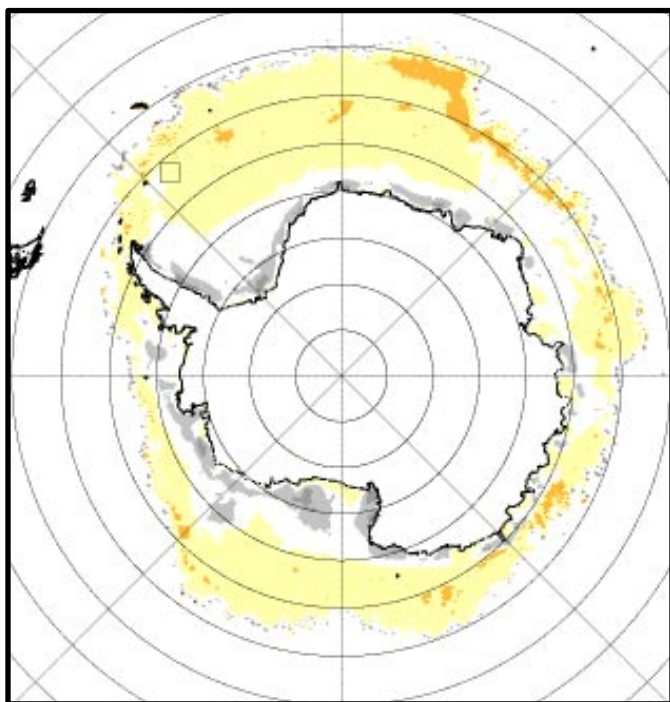**(a) Bootstrap Algorithm** September 18, 1988

(b) Revised Bootstrap Algorithm September 18, 1988
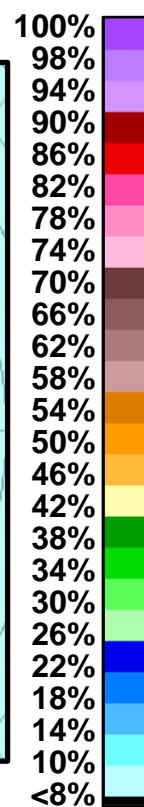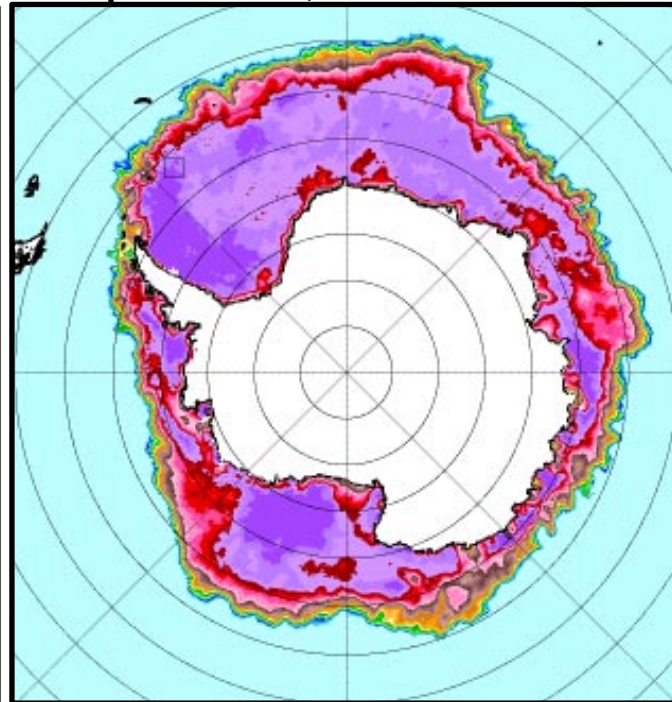
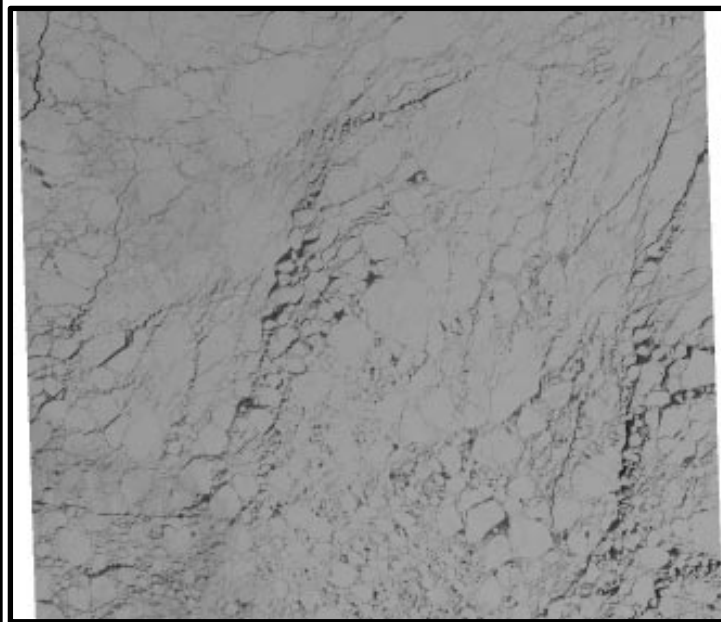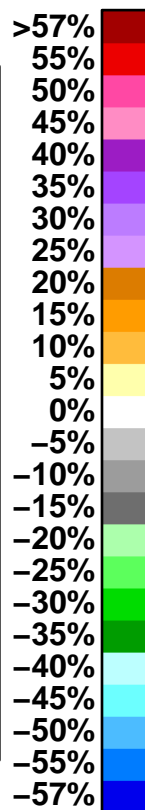**(c) Difference [(a) – (b)]**

(d) Landsat Image in Box

Figure 7.　(a) Ice concentration maps using the Bootstrap algorithm; (b) Ice concentration map using the temperature corrected Bootstrap algorithm; (c) difference between (a) and (b); and (d) Landsat data with in the rectangular box shown in (a) and (b).
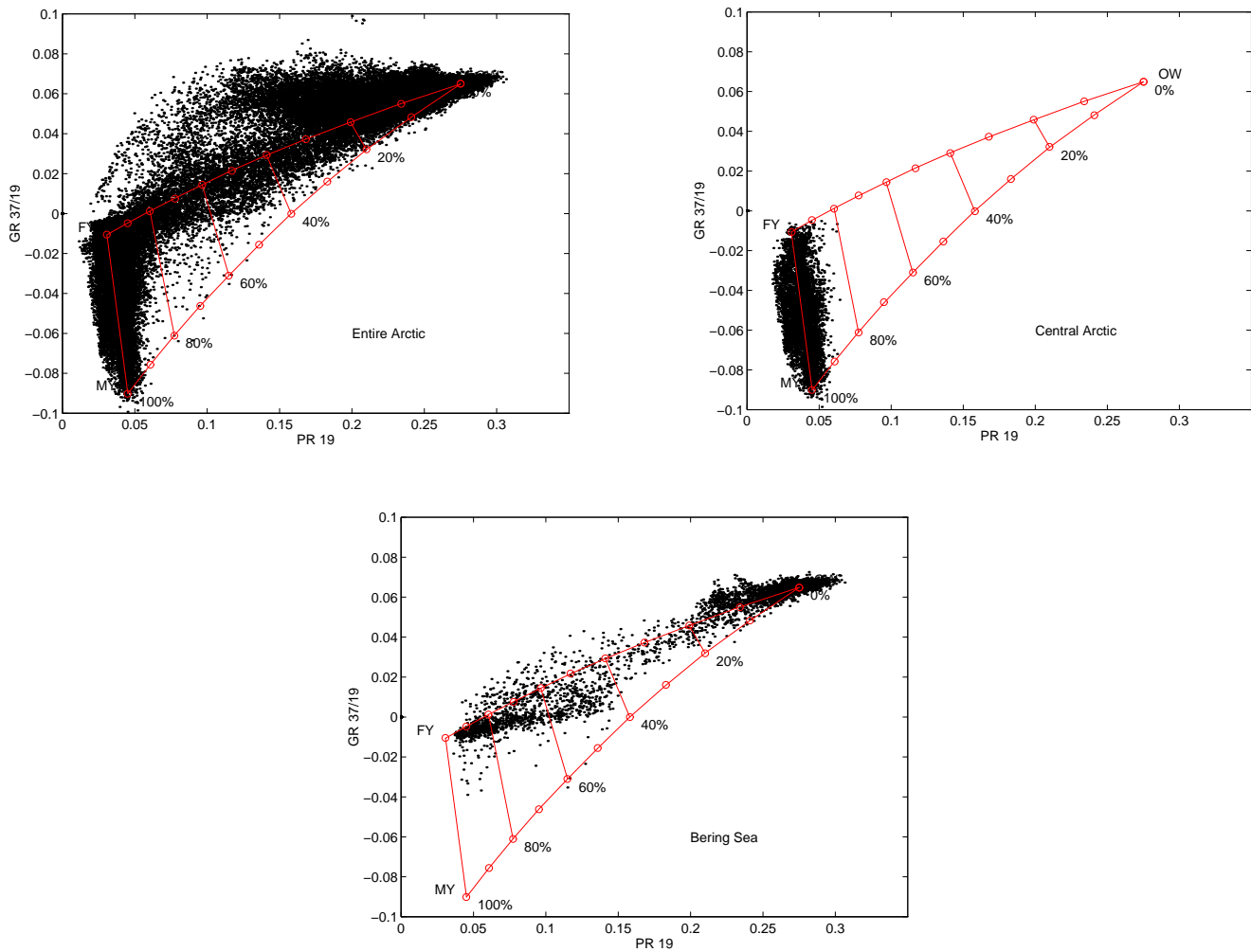
Figure 8.   PR–GR distributions for (a) the entire Arctic; (b) the central Arctic; and (c) the Bering Sea only. All for April 4, 1988 (after Cavalieri, 1994).

presence of new and young sea ice, reference is made to the Arctic PR–GR distributions for April 4, 1988 shown in Figure 8.   The distributions presented are for (a) ice–free and ice–covered oceans in the Northern Hemisphere; (b) the central Arctic region; and (c) the Bering Sea only. The algorithm triangle with labeled vertices and lines of constant ice concentration at intervals of 20% is superimposed on each of the three distributions.

In Figure 8a, the cluster of points representing ice–free ocean as well as weather related effects is located at the upper right vertex of the triangle labeled OW. The almost vertical cluster of points between the two other vertices corresponds to FY and MY ice types of high concentration. The cluster of points extending to the right of the FY ice vertex and having GR values close to zero is associated with new and young ice types. The horizontal spread of points in this cluster along a line nearly parallel to the PR direction depends on the age and thickness of the new ice. The position of this new and young ice cluster relative to the algorithm triangle (Figure 8a) explains why the algorithm underestimates ice concentrations in the presence of these ice types and why false indications of MY ice are often found in areas of new and young ice. At the right–hand end of this cluster (near the 40% isoline of concentration), the algorithm interprets the corresponding PR and GR values as an ice cover of about 45% concentration and of mostly MY ice.

For the central Arctic (Figure 8b), the cluster is almost vertical and has a relatively small degree of scatter (approximately ±10 percent) about the 100 percent ice concentration line. In contrast, the distribution for just the Bering Sea region (Figure 8c) consists of points clustered near the OW vertex and along the upper leg of the triangle (OW to FY). Points with GR values close to zero form a nearly horizontal cluster which cuts into the algorithm triangle. The other seasonal sea–ice zones contribute to the remaining portion of the totality of points shown in Figure 8a.

The distribution of points in Figure 8c is characteristic of seasonal sea–ice zones where there is little, if any, perennial ice and forms the basis of a new algorithm for determining the distribution of new, young and first–year ice types. A representation of this algorithm is illustrated in Figure 9 for the Bering Sea on April 4, 1988. The thin ice algorithm triangle is defined by (PR, GR) values for OW, FY and NEW ice. The cluster of points shown in Figure 8b for the central Arctic no doubt contains open water and thin ice, but cannot be resolved on scales comparable to the resolution of current satellite radiometers. Thus, the use of this algorithm is limited to seasonal sea ice zones and principally in the Bering Sea and similar regions.

Most of the points in Figure 9 fall between the 80% and 100% ice–concentration contours, indicating that this algorithm may provide an improved estimate of total ice concentration in regions of new and young ice. The relatively few points falling below the lower leg of the triangle are assigned concentrations of 100 percent. Their low GR values may result from volume scattering by deep snow accumulated in areas of ridged ice or on shore–fast ice adjacent to the coasts. A comparison of sea ice concentration maps for the Bering Sea for April 4 derived using the NASA Team algorithm and the thin ice algorithm is illustrated in Figure 10. Comparison of
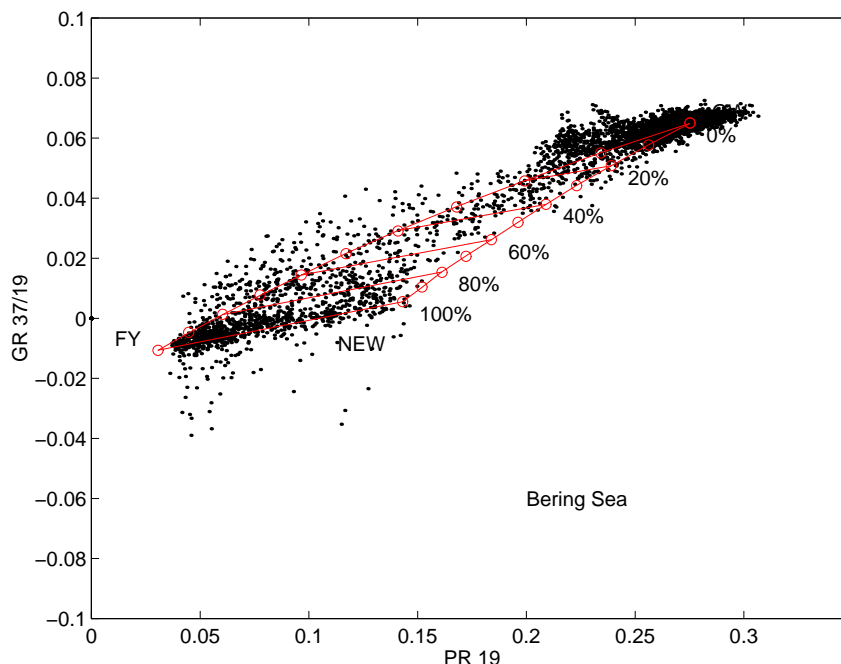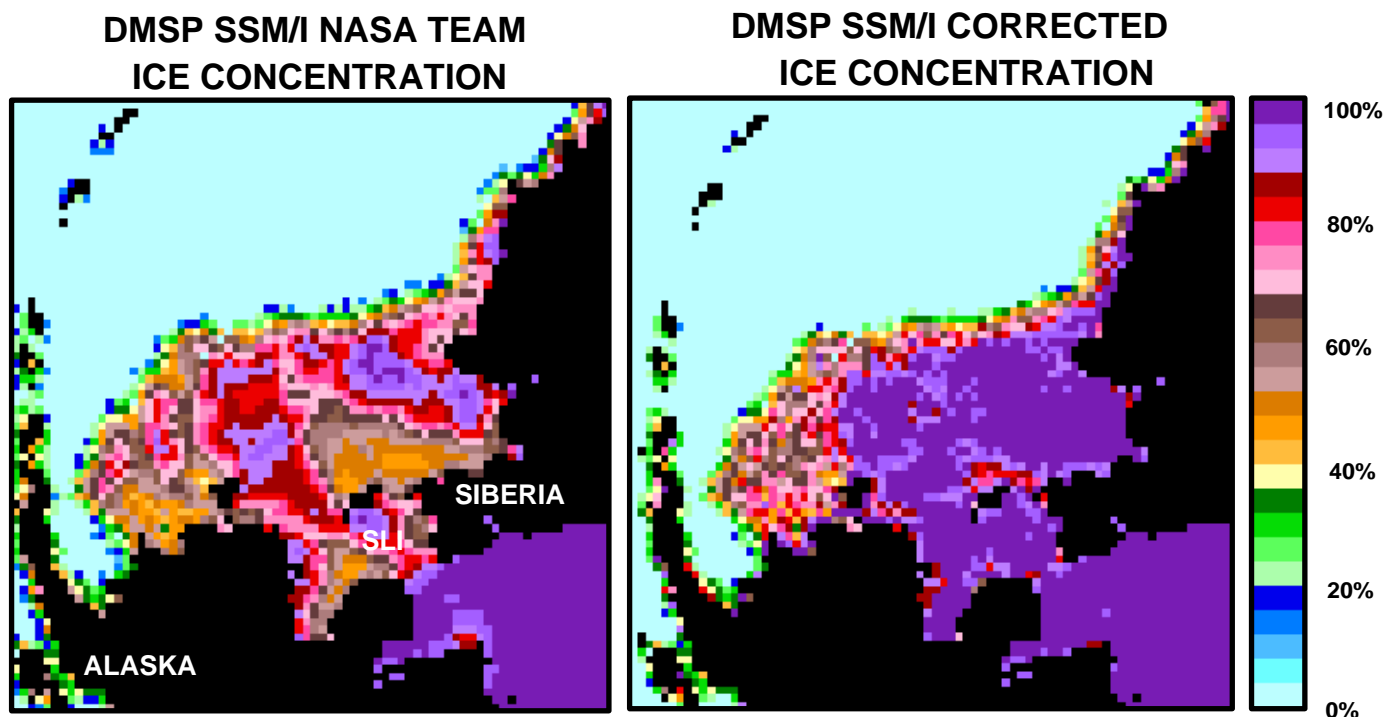

Figure 9. The thin ice algorithm is represented in (PR, GR) space by a triangle with vertices defined by open water (OW), first–year (FY), and new (NEW) ice points. The distribution of data points is for the Bering Sea on April 4, 1988 (after Cavalieri, 1994).

2 1

DMSP SSM/I NASA TEAM ICE CONCENTRATION

DMSP SSM/I CORRECTED ICE CONCENTRATION

SIBERIA

SLI

ALASKA

APRIL 4, 1988

Figure 10.   Bering Sea ice concentration maps for April 4, 1988, from (a) the NASA Team algorithm and (b) the thin ice algorithm.

the two maps shows that the thin ice algorithm yields substantially higher ice concentrations in the coastal polynya regions as indicated in the corresponding PR–GR plot (Figure 9). Higher ice concentrations in these regions are consistent with a supervised principal component analysis of DMSP SSM/I data which indicates OW concentrations of no more than 20–30% (Wensnahan et al., 1993) and by an ice–type classification of AVHRR imagery which shows that there is only a thin band of open water and new ice hugging the southern coasts of Alaska, Siberia, and St. Lawrence Island (see Plate 2c in Massom and Comiso, 1994). The sea ice concentrations in the southeast corner of the Bering Sea have not increased as much, suggesting that this is a low concentration area.

3.1.1.4 Correction for Weather Effects Over Ice–Free Ocean

With regard to atmospheric variability, the AMSR sea ice algorithm will employ a pair of weather filters to help eliminate spurious sea ice concentrations over ice–free ocean (Cavalieri et al., 1995).   The filters are based on threshold values for GR(37/19) and GR(22/19).   Ice concentrations for image pixels with GR(37/19) values greater than 0.05 and GR(22/19) values greater than 0.045 are set to zero.   This technique was originally used with GR(37/18) for eliminating weather effects in sea ice concentration maps derived from SMMR data (Gloersen and Cavalieri, 1986), and the addition of the second filter (GR(22/19)) was needed for the SSM/I sea ice concentration maps (Cavalieri et   al., 1995).   An alternative weather filter has been described by Comiso (1995) using a set of thresholds: one derived from the 19 GHz and 37 GHz data and another using the difference of 22 GHz and 19 GHz data at vertical polarization.   The strength of the latter is a consistent determination of the open water tie point that leads to a consistent ice concentration threshold for the weather filter.   When used independently, the two filters do not completely remove the spurious sea ice concentrations over ice–free oceans.   The

two techniques will be combined to enhance overall performance.

3.1.2 Sea Ice Temperature

Equation 10 provides the basis for calculating the temperature of the emitting surface. A map of emitting surface temperatures as inferred from equation 10 is shown in Figure 6d. The physical temperature of the ice component only, T_I, at the snow/ice interface, can be calculated using a mixing formulation and the derived ice concentration as done by Gloersen et al (1992). The same quantity can also be inferred directly from the equation:

$$T_I = (T_B - T_O)/C + T_O \qquad\qquad (16)$$

where T_B and T_O are the brightness temperatures of the data point and that of open water at 6 GHz. It is assumed that C is known. The two techniques will be used together for consistency checks.

The values obtained from SMMR using this method have been compared with results from the Temperature Humidity Infrared Radiometer (THIR) which measures surface temperature (Comiso, 1983). The surface temperature (skin depth) which is measured by THIR can be substantially different from the ice temperature which is measured by SMMR (or AMSR). To convert the THIR values to snow/ice interface values, we use a regression model based on field measurements (Comiso et al., 1989). The average values from THIR and SMMR were comparable (within 5K in much of the Antarctic region(see Figure 11)). However, while the THIR results show a monotonic progression of increasing temperatures from the continent to the ice edge, the coldest temperatures from SMMR were in the middle of the ice pack. This may have been caused partly by spatial variations in snow cover which were not taken into account in the conversion algorithm for the THIR data. More extensive validation of the resulting temperatures will be made. However, it is encouraging that the SMMR temperature appears to improve the distribution of consolidated ice in the scatter plots.

3.1.3 Snow Depth on Sea Ice

Although surface and aircraft observations suggest that the 85 GHz data may be useful for developing a snow depth algorithm (Grenfell, 1986; Cavalieri et al., 1986; Comiso et al., 1989), comparative analyses of in situ snow depth measurements with nearly coincident SSMI observations at 85 GHz show that this is not the case. We attribute this to the sensitivity of the 85 GHz channels to the variability of the intervening atmosphere even over fairly consolidated sea ice (Markus and Cavalieri, 1996). Current algorithms to derive snow depth over land use the difference between the brightness temperatures at 19 GHz and 37 GHz both at horizontal polarization (Kunzi et al., 1982; Chang et al., 1987). This work suggests that these channels may also be useful for developing a snow–depth algorithm for sea ice. Grenfell and Comiso (1986) measured brightness temperatures at frequencies between 10 and 37 GHz before and after a snowfall on saline, 3.5 cm thin ice. The largest effect was seen at the 37 GHz H–pol. where the emissivity was reduced from about 0.76 for bare ice to 0.59 after a 4.5 cm snowfall. The emissivity difference between bare ice and snow–covered ice at 19 GHz H–pol., 19 GHz V–pol., and at 37 GHz V–pol. was about 0.04.

The snow depth algorithm starts with the linearized radiative tranfer equation, used above for the sea ice concentration algorithms, where measured brightness temperature at frequency ν

(a) Ice Temp.
   Sept 15, 1979

>278 K
276 K
274 K
272 K
270 K
268 K
266 K
264 K
262 K
260 K
258 K
256 K
254 K
252 K
250 K
248 K
246 K
244 K
242 K
240 K
238 K
236 K
234 K
<232 K

(b) THIR Temp.
   Sept. Avg.

>278 K
276 K
274 K
272 K
270 K
268 K
266 K
264 K
262 K
260 K
258 K
256 K
254 K
252 K
250 K
248 K
246 K
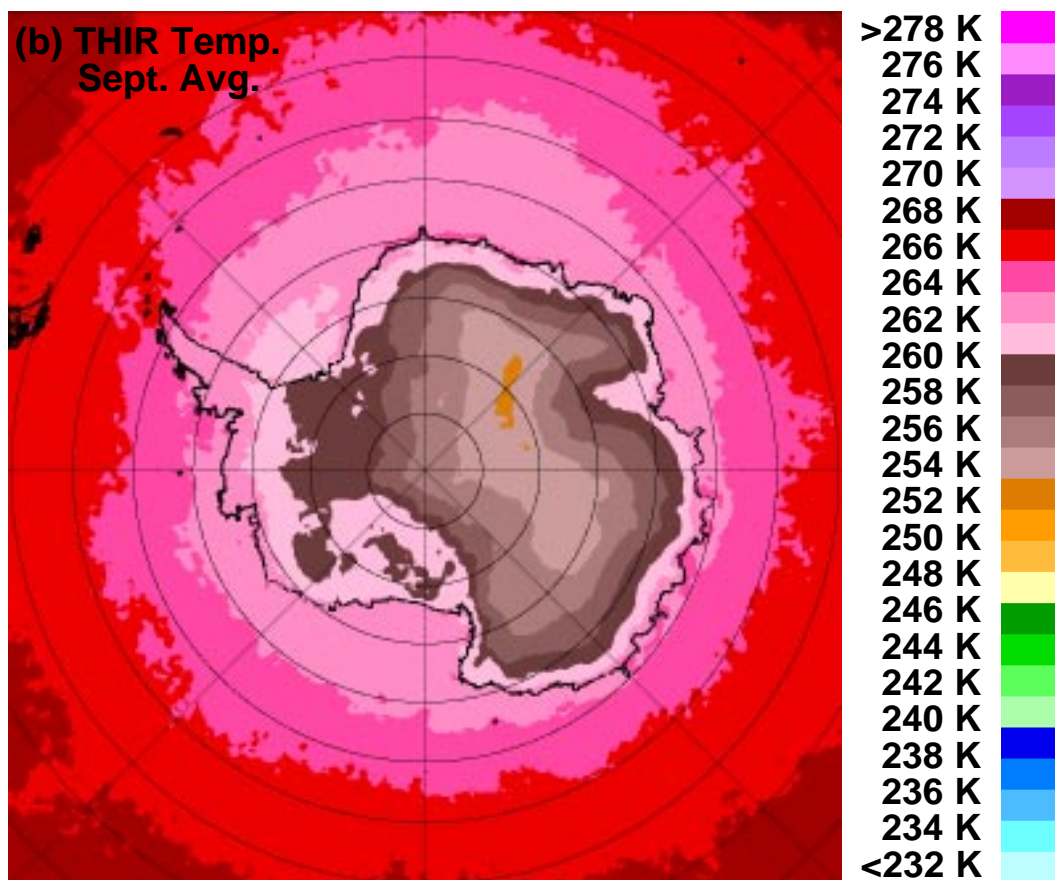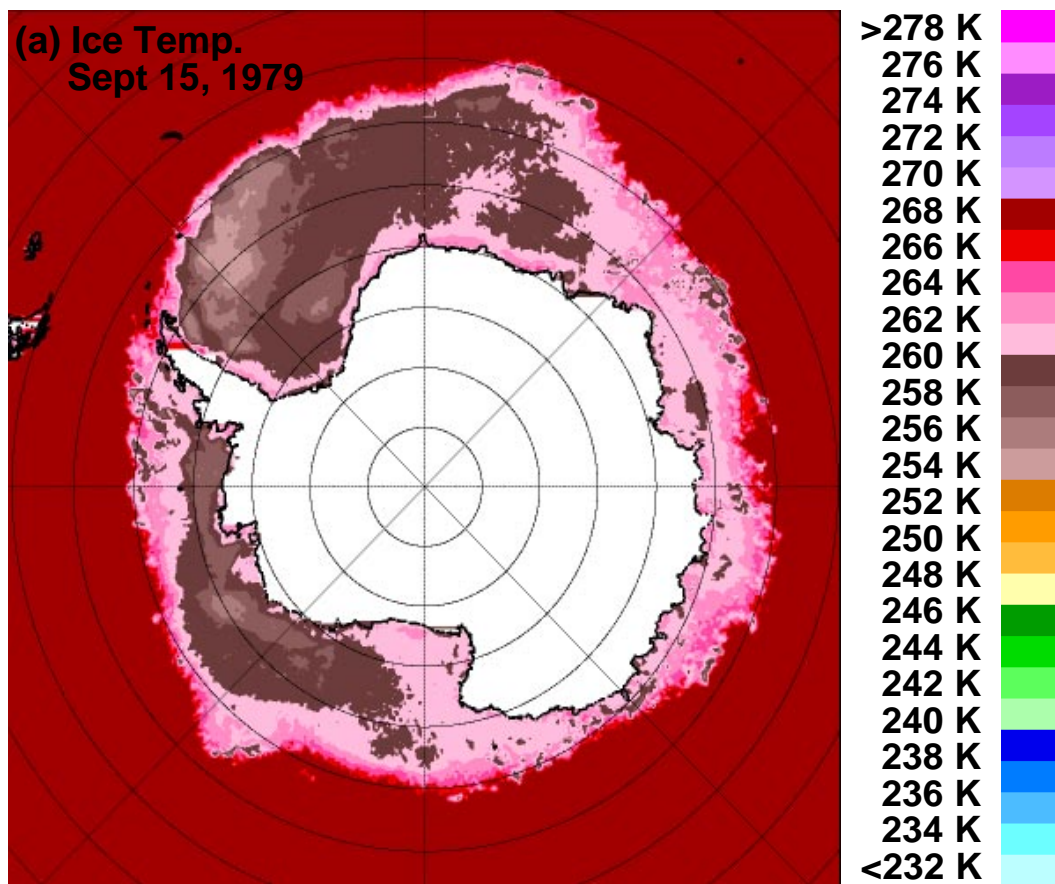244 K
242 K
240 K
238 K
236 K
234 K
<232 K

Figure 11.   (a) Ice temperature data derived from the 6 GHz channel and (b) Ice temperature inferred from the THIR surface temperature data.

and polarization component p, TB(ν,p), consists of a mix of brightness temperatures for open water $T_{BW}(\nu,p)$ and sea ice $T_{BI}(\nu,p)$

$$T_B(\nu,p) = CT_{BI}(\nu,p) + (1-C)T_{BW}(\nu,p) \tag{17}$$

where C is the ice concentration. The value of C is computed using the procedure discussed in the previous section. The open water brightness temperature T_{BW} is an average value over the open ocean regions for each channel and is assumed to be constant. Because we are only interested in changes of brightness temperature resulting from changes in snow cover on sea ice, open water is excluded from the signal. From this equation T_{BI} is calculated and used later in the snow algorithm. Changes in T_{BI} are assumed to reflect changes in snow depth.

Next, temporally coincident in situ snow–depth and SSMI measurements were used to derive a linear relationship between snow–depth and SSMI observations. The specific data sets used in the analysis are given in Markus and Cavalieri (1996). The in situ data represent a wide range of regions and seasons in the Antarctic. Nonetheless, the areal coverage of these surface measurements is still small compared to an area of about 625 km^2 for a single SSMI image pixel. The actual snow depth variability over an SSMI pixel is uncertain. Different combinations of channels for TB_I were tried in the regression. Combinations using the 85 GHz channels resulted in average differences that were twice as large (approx 13 cm) as those using the 19 and 37 GHz combination (7 cm). The use of GR (H). or GR (V). gave better results than the unnormalized difference. While GR (H). and GR (V). gave similar average differences, we decided to use the horizontal channels because of previous work indicating that these channels were particularly sensitive to snow cover variability (Kunzi et al., 1982; Grenfell and Comiso, 1986; Chang et al., 1987). It is noteworthy that these channels have already proven useful in previously derived land snow algorithms and that the vertically polarized spectral gradient ratio is known to be influenced by snow cover on sea ice (Cavalieri et al., 1991). Fig. 12 shows a scatter plot of measured snow depth versus $GR_I(H)$, where GR_I (H) is defined by:

$$GR_I(H) = (T_{BI}(37H) - T_{BI}(19H))/(T_{BI}(37H) + T_{BI}(19H)) \tag{18}$$

Besides the expected scatter a clear linear relation between $GR_I(H)$ and snow depths can be seen. Furthermore, the relationship is consistent for all four campaigns although they cover different regions and seasons. Also the range of snow depths is very different. Measurements from Jeffries lie between 0 and 30 cm, whereas the measurements from Ackley range from 40 to 70 cm. An interesting feature can be seen in the data set of Worby and Massom (1995). Two separate linear clusters of points labeled by empty boxes and boxes with crosses can be distinguished. The line with higher $GR_I(H)$ values (boxes with crosses) are associated with higher surface air temperatures between 0 and –6C. This higher $GR_I(H)$ signature may result from wet snow or snow having larger grains, which reduces the scattering at one frequency relative to the other (Chang et al., 1976), but the amount of data is too small to give a clear relationship between temperature and passive microwave signal. The selected regression fit does not include these points. The linear regression fit is given by

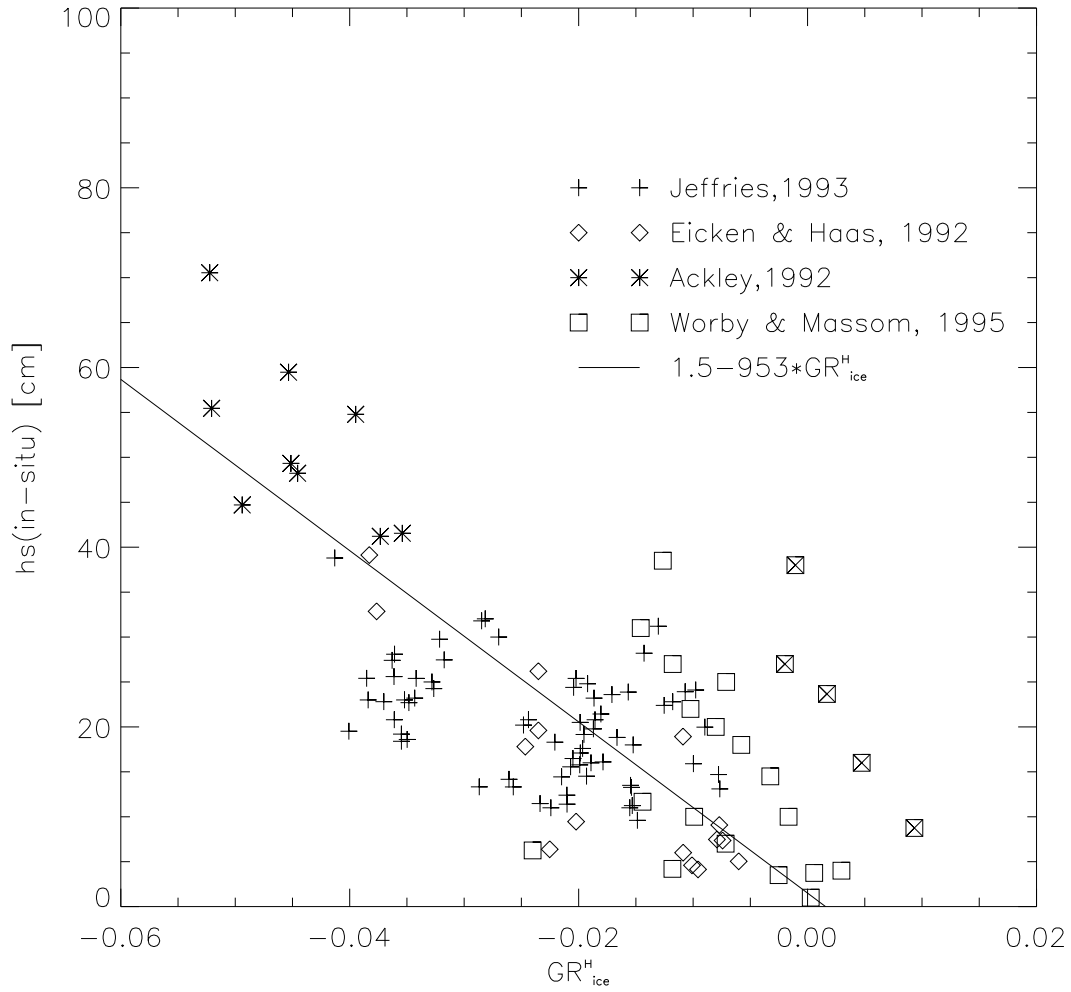$$h_S = 1.5 - 953 * GR_I(H) \tag{19}$$

Figure 12.   SSMI GRHice versus in situ snow depth measurements (after Markus and Cavalieri, 1997).

and is plotted in Figure 12. The brightness temperatures for open water at the 19 and 37 GHz horizontally polarized components are 106.8 K and 139.3 K respectively.   The complete algorithm combining equations (17), (18), and (19) can be written explicitly as

$$h_s = 1.5 - 953*(T_B(37H) - T_B(19H) - 32.5(1-C))/(T_B(37H) + T_B(19H) - 246.1(1-C)) \qquad (20)$$

The standard error of estimate about the linear regression line is 7 cm. Using this algorithm, monthly mean Antarctic snow depths were calculated using seven years (1988–1994) of DMSP SSMI data and are presented in Figure 13.

In the Arctic the retrieval of snow depth is complicated by the presence of multiyear ice which has a signature similar to the snow cover. Both multiyear ice and deep snow result in more negative values for GR. Until we are able to discriminate between variations in multiyear ice and variations in snow depth, snow depth will only be retrieved in regions where the multiyear ice concentration is less than 20% (false indications of MY ice of up to 20% have been observed in SSIZs). Additional channels and greater spatial resolution provided by AMSR may help in this regard.   Cross comparisons between SSMI and ADEOS–II AMSR brightness temperatures
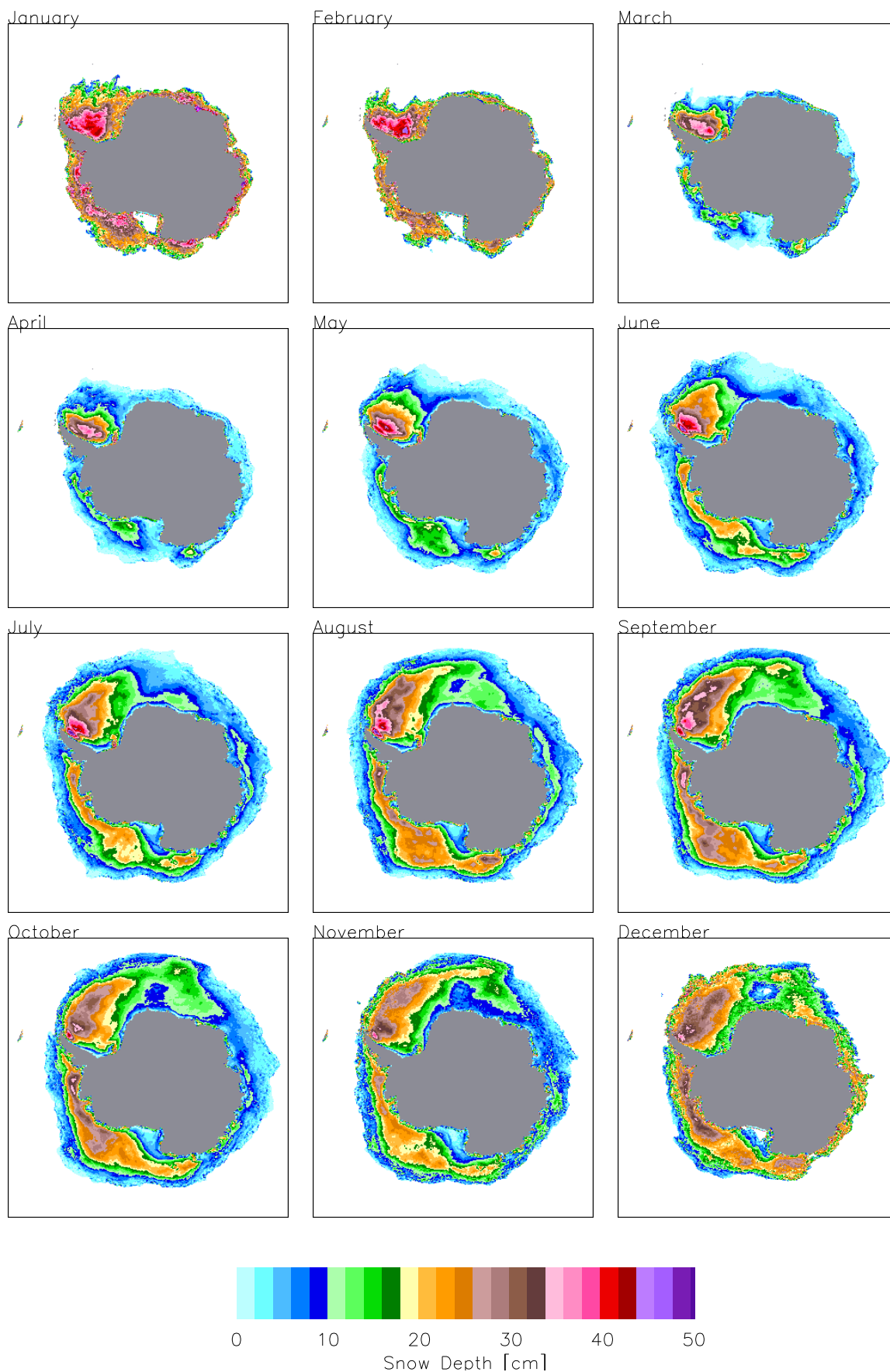
2 6

Figure 13. Mean monthly Antarctic snow depths based on seven years of DMSP SSMI data.

should help us tune the algorithm coefficients for the Antarctic and in the Arctic SSIZs.

3.2 Special Products

3.2.1 Sea Ice Motion

A new method of time–varying signal analysis, called the Wavelet Transform, has been used for image processing applications at NASA/GSFC during the past three years (Liu et al., 1995; Peng et al., 1995). Basically, wavelet transforms are analogous to Fourier transforms, but are localized both in frequency and time. Wavelet analysis has been recently applied to SSMI 85 GHz radiance maps to obtain daily sea ice drift information for both the northern and southern polar regions (Liu et al.,1996). This technique provides improved spatial coverage over the existing array of Arctic Ocean buoys and better temporal resolution over techniques utilizing data from satellite synthetic aperture radars.

The method utilizes a two–dimensional Gaussian wavelet as an edge detector to identify ice features in SSMI imagery. These features are then tracked from day to day. The use of this technique has been demonstrated through a comparison with ice displacements derived from Arctic and Antarctic drifting buoy data. Application of this technique to Arctic SSMI 85 GHz radiances for December 12, 1992 results in the ice displacement map shown in Figure 14a. The white arrows in the figure represent the ice drift computed from feature displacements from December 11 to December 13, 1992. Examination of the figure shows two well–known Arctic ice–drift features: the Beaufort Gyre and the Transpolar Drift Stream. The dark arrows indicate the corresponding ice displacements computed from ice buoy data also from December 11 to December 13, 1992 and are consistent with both the direction and magnitude of the white arrows. The technique was also applied to data for mid January 1993. The result is shown in Figure 14b. A comparison of Figures 13a and 13b shows a remarkable change in the ice drift pattern. The Beaufort Sea ice drift is now counter–clockwise as is the whole circulation pattern of the Arctic Basin. Again a comparison with the Arctic Ocean buoy data (dark arrows) shows good overall agreement.

Further development of this technique for use with passive microwave data is needed to optimize its use for extracting ice drift information. Comparisons with other techniques would also be useful. Comparison data sets for assessing the present technique include Arctic and Antarctic buoys, AVHRR–derived ice motion, and output from the RADARSAT Geophysical Processing System. Based on this preliminary assessment, we anticipate that wavelet analysis of AMSR imagery will help to improve our current knowledge of sea ice drift and related processes for both polar regions. This wavelet analysis procedure is robust and can make a major contribution to the understanding of ice drift over large areas at relatively high temporal resolutions. This new source of ice drift data offers a potential solution to the problem of inadequate temporal sampling. Pairs of daily AMSR images can provide ice displacements every day greatly increasing the temporal sampling.

3.2.2 Arctic Sea Ice Types

In the Arctic we obtain first–year and multiyear ice concentrations from Equations (4) and (5) respectively. Maps of multiyear ice concentration (CMY) and a discussion of the accuracy of its retrieval is given in Cavalieri et al. (1991) and Gloersen et al. (1992). A map of multiyear sea
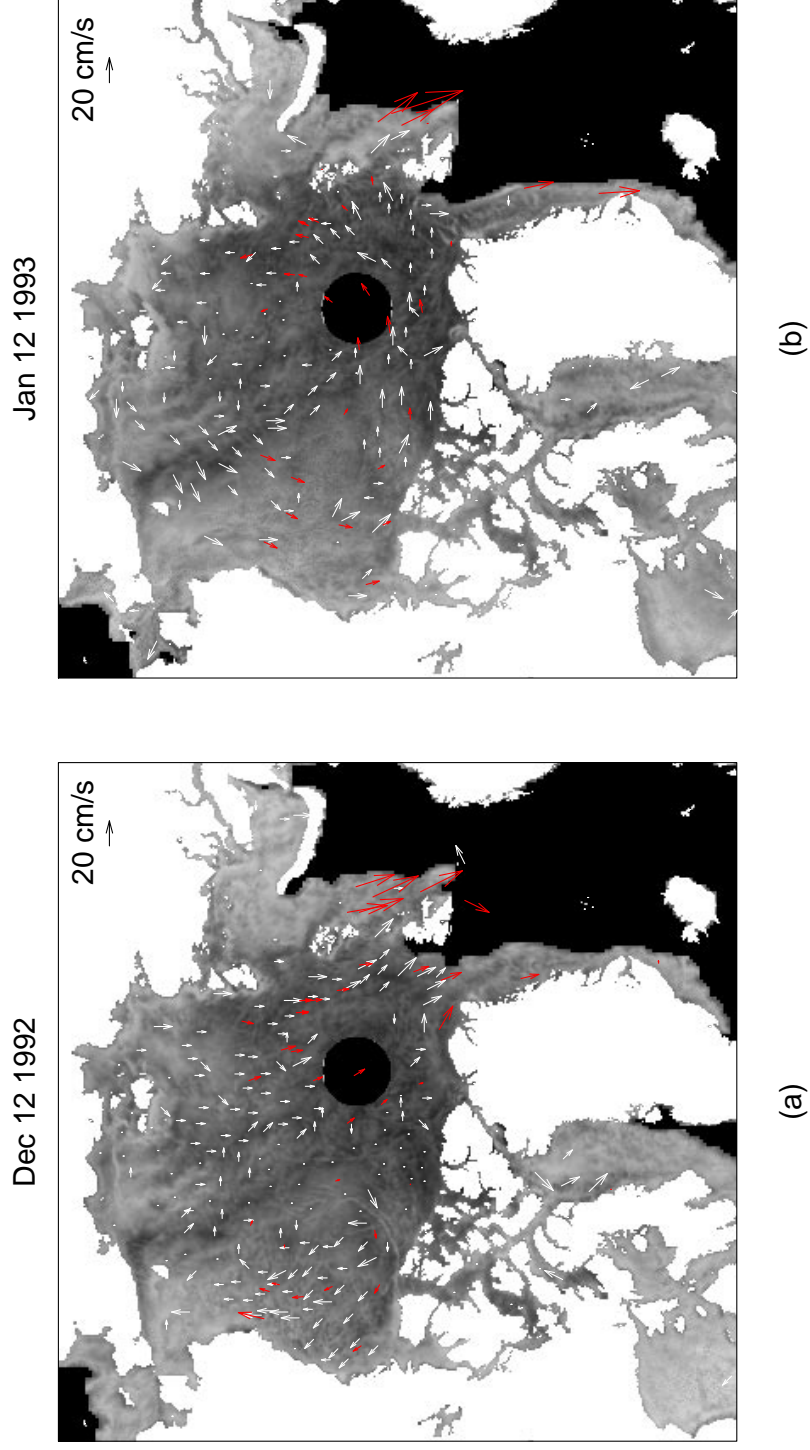
Figure 14. Sea ice displacement vectors calculated using the wavelet transform technique applied to SSMI 85 GHz data (white arrows) and ice displacement vectors derived from Arctic Ocean buoy data (red arrows) are shown for (a) December 12, 1992 and (b) January 12, 1993.

April 4, 1988

NOAA AVHRR

NOAA AVHRR Ice Type

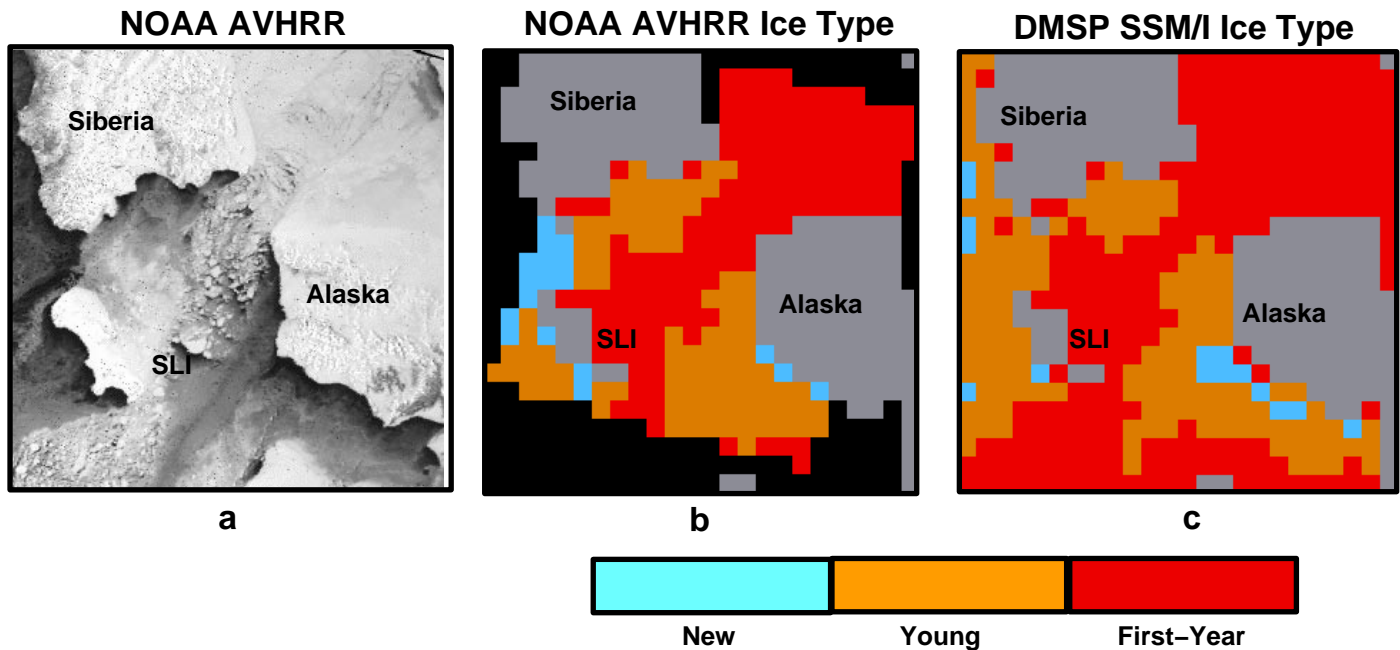**DMSP SSM/I Ice Type**

a

b

c

| New | Young | First–Year |

Figure 15. (a) NOAA AVHRR (channel 2) image of St. Lawrence Island and vicinity, (b) DMSP SSMI ice type map. All for April 4, 1988 (after Cavalieri, 1994).

ice concentration is illustrated in Figure 3. In Arctic seasonal sea ice zones, the ice types that are present consist of first–year and younger types. An algorithm for mapping new, young, and first–year sea ice distributions has been developed (Cavalieri, 1994), but validation has been limited to the Bering Sea. The variation of PR(19) with ice type serves as the basis for mapping the ice types. A nomogram (not shown) that relates the PR, calculated with the 19–GHz SSMI channels, and the corrected total ice concentrations obtained from the thin ice algorithm, is used to determine ice type. The ice type distribution for the Bering Sea derived using this method is compared with an AVHRR–derived distribution in Figure 15. For the AMSR, once the enhanced total sea ice concentration is calculated, a similar the nomogram will provide an estimate of the ice type. The exact range of PR for each ice type is still uncertain, but the values used here are in reasonable agreement with the field observations.

3.2.3 Sea Ice Surface Classes

Another parameter of interest is a classification of the ice cover in terms of regional surface classes which are sometimes referred to as ice regimes (or zones). Different ice regimes may be associated with physical boundaries such as between the outer and inner zones, between seasonal and perennial zones, and between divergence and convergence zones. The outer zone, which includes the marginal ice zone, is perhaps the easiest to identify in the passive microwave data because of the marked contrast in emissivity between the ocean and ice covered regions at some frequencies. It is also characterized as the region where loose pancakes are located and where the effect of waves dominate. The inner zone, on the other

hand, is the region where the ice cover is practically a continuous sheet of ice except where there are leads and polynyas. In the inner zone, there can be a divergence zone in which large number of leads are formed or a convergence zone where extensive rafting and ridging occur. Also, within the pack there are perennial zones which are areas where icefloes survive the summer. Such zones may have different signatures in different areas depending on age and extent of deformity.

Cluster analysis of the multichannel passive microwave data (SMMR and SSMI) have indicated that data points from the same ice regime tend to cluster together, suggesting that they are radiometrically distinct. An unsupervised cluster analysis software, called "Isoclass", has been used to identify and separate these radiometrically distinct clusters (Comiso, 1990; Comiso 1996). The general technique was developed by several groups (Ball and Hall, 1967; Kan, 1973; Wharton and Lu, 1987) leading to the Land Analysis System (LAS) and has been implemented for general remote sensing applications by some commercial software companies (e.g., PCI Remote Sensing Corp.).

Details about the current technique as applied to SSMI data, including refinements using a neural network system, are discussed in Comiso (1996). Ten different classes including open water have been identified. To illustrate the effectiveness of the classification, weekly cluster maps from autumn (October 1993) through mid–winter (January 1994) are shown in Figure 332a. Our interpretation of the color code representing each radiometrically distinct cluster is as follows: A for open water, B and C for new or loose pancake ice mainly in the marginal ice zones, D for young ice, E and F for first year ice, and G, H, I, and J for multiyear ice. Class F may be partly multiyear ice but is believed to be primarily first year ice with thick snow cover. The cluster maps show patterns in the inner zone that are generally stable and similar to characteristic distribution of ice floes based on buoy data by Colony and Thorndike (1985). The time development pattern in the seasonal region and the marginal ice zones also appear consistent with that expected during the period. In this region, some transformations from one class to another occur as new ice (B and C cluster) forms and turns into young ice (D cluster) which then turns into first year ice (E or F cluster) in a matter of several days. The progression of this sequence can be monitored with the weekly cluster maps. The maps in Figure 15 indicate that much of the changes in the Arctic cover during winter is primarily due to ice growth. The areal cover of the marginal ice zone is estimated to be almost constant indicating that the amount of ice in the ice margins does not change much although the ice edges change in location during the season. Changes are thus primarily due to increases in young and first year ice cover.

Changes in shape and location of the various surfaces during the season are apparent. The general movement is consistent with forcings associated with average wind directions and movements of the Arctic gyres. In a sense, the movements of basic ice regimes provide a means to quantify the large scale dynamics of the Arctic and other regions. The maps also provide a means to evaluate how the various regimes changes from one year to another. These maps can thus be very useful for mass balance and thickness distribution studies and for testing large scale ice models.

3.3 Uncertainty Estimates

In the following sections we will discuss estimates of uncertainties based on previous in situ and validation studies in limited areas and time periods for the NASA Team and Bootstrap algorithms separately. The results of sensitivity studies are also presented. Our current

estimates will be updated after a validation study of the AMSR hybrid algorithm has been implemented using simulated and real AMSR data.

3.3.1 Sea Ice Concentration

A NASA sea ice validation program for the NASA Team algorithm using DMSP SSMI data was initiated in 1987 and was completed in 1991. Results of the SSMI Sea Ice Validation Program have been published in a final report (Cavalieri, 1992) and in three journal publications (Cavalieri, 1991; Cavalieri et al., 1991; Steffen and Schweiger, 1991). Validation of the SSMI sea ice products centered on comparative analyses of multisensor satellite and aircraft data sets including LANDSAT MSS and NOAA AVHRR; aircraft sensors included C–, L–, and P–band SAR, a Ka–band scanning radiometer, a fixed–beam multichannel radiometer, and aerial cameras. The results from the Landsat comparisons, which covered all seasons and both hemispheres, showed that, on average, the difference between the NASA Team algorithm using SSMI data and the Landsat derived ice concentrations was –3.6%±6.6% for winter months, whereas for early spring in the Amundsen Sea the result was 1.3%±3.6%.

The physical basis of the Bootstrap algorithm has been confirmed using ground based radiometer experiments in the Antarctic and in controlled experiments at the Cold Regions Research Laboratory (Comiso et al., 1989; Grenfell et al., 1994; Grenfell and Comiso; 1986). Comparative studies with aircraft, SAR, Landsat, and Helicopter data have also been made indicating consistencies generally within 5% in winter and higher in the summer, and confirming validity of the assumptions (Comiso et al., 1984; Comiso, 1986; Comiso et al., 1991; Comiso and Kwok, 1996).

Monthly sea ice concentration maps derived from the NASA Team and the Bootstrap algorithms have been analyzed and compared for an entire year in Comiso et al. (1997). The AMSR algorithm is a hybrid algorithm making use of both the NASA Team algorithm and an enhanced Bootstrap algorithm, which takes advantage of the 6 GHz AMSR channel to minimize effects resulting from spatial changes in ice temperature.

3.3.1.1 Physical Temperature Variations

In the NASA Team algorithm, the derived ice concentrations are, to first order, independent of spatial and temporal variations in ice temperature through the use of ratios of brightness temperatures, PR and GR. The potential sensitivity of GR to ice temperature variations has been discussed elsewhere and is not expected to be a problem (Gloersen et al., 1992; Comiso et al., 1997).

In the Bootstrap algorithm, the use of the HV37 set of channels (for concentrations >90%) helps reduce the error resulting from spatial changes in the snow/ice interface temperature in the retrieval of ice concentration. In the HV37 scatter plot, the slope is about 1.0 for consolidated ice data. Thus, changes in physical temperature cause almost equal changes in brightness temperature for both polarized components, with the result that data points move almost along the line AD (Figure 4). Sensitivity to random changes in ice temperature of 15K and 30K are shown in Figures 4c and 4e, respectively. These plots indicate that even with large spatial variations in snow/ice interface temperature in the perennial ice pack of the Arctic region in winter, the effect on the accuracy in the determination of ice concentration is very small.

In the Antarctic region and part of the seasonal regions in the Arctic where the V1937 set is

utilized, the effects of changes in the surface temperature are not as well taken into account because the slope of the reference line, AD, is about 0.47 to 0.62, compared to near 1.0 for the HV37 set. The difference in slope is due mainly to different volume scattering effects at different frequencies. The scatter plot shown in Figure 4b shows greater variability of data points along the consolidated ice cluster (i.e., AD) than that of Figure 4a. The scatter of data points along AD is due to the spatial variabilities in both snow/ice interface temperature and in emissivity. Deviations in ice concentration from 100% due to the presence of leads in the region are also reflected in this variability. Sensitivity to random changes in snow/ice temperatures of 15K and 30K are simulated and shown in Figures 4d and 4f, respectively, for the V1937 set. These latter plots indicate that the effect of changes in snow/ice surface temperatures of these magnitudes may indeed be large.

A sensitivity analysis using the HV37 set of channels results in a 0.05% change in ice concentration per Kelvin change in physical temperature. Using the V1937 set of channels, the sensitivity is about 0.9%/K in the Antarctic, whereas in the Arctic the corresponding value is 0.84%/K. With the enhanced Bootstrap Algorithm, which makes use of emissivity instead of brightness temperature data, such errors are expected to be considerably reduced. However, significant errors are expected at boundaries, especially in the Marginal Ice zone and the coastal boundaries where the matching of the footprints from different channels are critical because of highly contrasting emissivities. At the ice edge, the spatial changes in surface temperature are expected to be small, because both the ice temperature as well as the sea surface temperature are likely to be close to 271 K.

3.3.1.2 Ice emissivity variations

For the purpose of comparing the sensitivity of each algorithm to potential variations in surface emissivity, the brightness temperature for the channels used by each algorithm was varied by ± 1 K and the ice concentration was computed. The results are presented in Comiso et al. (1997) for both the Bootstrap and Team algorithms. Under conditions of 100% ice cover, the Bootstrap algorithm shows a sensitivity ranging from 1.7% to 2.2% depending on hemisphere, while the Team algorithm sensitivity is 1.8% for both hemispheres. For a 50% ice cover, the Bootstrap algorithm yields a sensitivity ranging from 0.8% to 1.1% and the Team algorithm sensitivity is 1.2%. Based on this study, the differences in sensitivity to emissivity variations between the two algorithms are not significant.

The horizontally polarized channels may be more sensitive to snow structure and other surface effects than the vertically polarized channels as has been reported by Matzler et al., (1984) from surface observations. Further research is needed to determine if this effect is observed from a satellite platform and will be an integral part of the validation study.

3.3.2 Sea ice temperature

The brightness temperature distribution at 6 GHz in areas where the ice concentration is greater than 95% in the Arctic and the Antarctic have been observed to have standard deviations of 2.8K and 3.0K, respectively. The distribution includes effects resulting from spatial variations in temperature and emissivity. For a typical brightness temperature of 250 K and ice temperature of 260 K, the emissivity would be 0.96. Since the observed fluctuations in snow/ice interface temperature is about 2.5 K (Comiso et al., 1989), the standard deviation of the emissivity is about 6. If we assume that the uncertainty in the emissivity of ice is 0.6% and the uncertainty in the brightness temperature is 1K, the error in the determination of the physical

temperature of near 100% ice would be 0.72% of the physical temperature (typically about 2K).

In areas where the fraction of open water is significant, the error becomes larger, especially because the emissivity has to be calculated using equation 9, which provides only an approximate value. Incorporating the error in this equation, a typical error in the emissivity is 0.86%. Again, by assuming that the uncertainty in the brightness temperature is 1K, the error in the determination of the physical temperature at 50% ice concentration would be .95% of the physical temperature (about 2.5K).

Although biases in the calibration contributes to additional error, this will be minimized by using the satellite data (in conjunction with in situ measurements) to obtain estimates of the effective emissivity near 100% ice concentration. Also, relatively large footprints causes uncertainties near the boundaries (i.e., sea ice and open ocean, and sea ice and land). Furthermore, the temperature represents that of the snow ice interface in the seasonal region while it represents a thicker layer (i.e., above the freeboard) in the perennial ice region.

3.3.3 Snow depth on sea ice

Input parameters to the snow algorithm are the brightness temperature of 19 GHz and 37 GHz both at horizontal polarization and the ice concentration. The sensitivity of the snow depth retrievals to ice concentration variability was investigated as follows. We took a sample data set of brightness temperatures from actual data containing over 30,000 pixels and introduced a trial error in ice concentration. The results indicate that the snow depth is sensitive to errors in ice concentration. Except for ice concentrations of 20% or less, the sensitivity is below 1 cm/% with a minimum at 50%. The greater sensitivity at concentrations of 20% and less might result from the greater influence of weather effects in regions with low ice concentration. We therefore limit the allowable ice concentration to the range between 20% and 100%. If the ice concentration is below 20% the snow depth is set to 0 cm. We conclude that errors in ice concentration have little effect on the snow depth estimate.

Gloersen and Campbell (1988) have observed in airborne observations, and Maslanik (1992) has shown in a theoretical study of weather effects on ice concentration retrievals, that at higher ice concentrations weather effects increase GR whereas PR is less affected. This greater effect on GR might also be reflected in the snow depth calculations. A quantitative estimate of this error needs to be computed

Grain size variability will affect the GR_lH and lead to errors in the calculation of snow depth. In a theoretical study of the effect of snow grain size on microwave emission, Chang et al. (1976) show that at 19 GHz even a small decrease in grain size from about 2 mm to 0.1 mm will greatly increase the emitted brightness temperature for snow depths greater than 20 cm. This sensitivity is even greater at 37 GHz for grain sizes less than 1 mm. Given a mean grain size of 1.7 mm for snow cover on Antarctic sea ice (Worby and Massom, 1995), the brightness temperature at 19 GHz $T_B(19)$ will be much more susceptible to grain size variability than the brightness temperature at 37 GHz $T_B(37)$. Higher values of $T_B(19)$ relative to $T_B(37)$ will result in a GR decrease and thus in an overestimate of snow depth. Conversely, larger than average grain sizes will lower $T_B(19)$ values relative to $T_B(37)$ resulting in an underestimate of snow depth. Also the grain size of newly fallen snow increases with time (Lohanick, 1993). Older snow will lead to an underestimate of snow depth, whereas new snow depth will be overestimated. Although variation in grain size can cause changes in brightness temperature of more than 50 K,

the importance may be reduced because of large–scale averaging. On the other hand, Josberger et al. (1996) have shown significant interannual variability of average grain size.

3.3.4 Special Products

Sea Ice Motion

A comparison of ice displacements determined by the wavelet transform technique with those determined from Arctic Ocean ice buoys for December 12, 1992 (Figure 14a) provided a measure of accuracy. Ice velocities of wavelet derived features within 8 km of 27 buoys were determined. The ice speed differences between the ice features and the 27 buoys have a mean value of 3.9 cm/s with a standard deviation of 2.6 cm/s. The direction differences have a mean value of 27.5^O with a standard deviation of 25.9^O. For the January 1993 example (Figure 14b), the ice speed differences between the wavelet derived features and 24 buoys has a mean value of 2.7 cm/s with a standard deviation of 2.9 cm/s. The direction differences have a mean value of 27.0^O with a standard deviation of 18.0^O. Similar results are obtained for the Antarctic (Liu et al., 1996). The accuracy of this technique is only limited by the persistence of the features and by the spatial resolution of the sensor. For example, a feature displaced 12.5 km (the SSMI grid spacing for 85 GHz) over 2 days will have a computed speed of 6.25 km/day (7.2 cm/s). In this case, the uncertainty in the estimate is 3.6 cm/s which agrees with the quantitative estimates of the differences between the wavelet derived features and buoys in given above.

Arctic Sea Ice Types

The uncertainty in C_{MY}, estimated to be about 11% (Cavalieri et al., 1991), is considerably larger than the estimate for total sea ice concentration. False indications of multiyear ice of up to 20% have been observed in seasonal sea ice zones. Nonetheless, C_{MY} is considered useful for sea ice model validation studies. In a study of model– and satellite–derived multiyear ice concentrations, Walsh and Zwally (1990) show that simulated multiyear ice concentrations are slightly higher than the satellite–derived concentrations, but the total coverage of the simulated multiyear ice agrees well with the satellite–derived coverage. They show that both the simulated and satellite–derived coverages in the early 1980s show large interannual variations that represent potentially large perturbations in the mass balance of Arctic pack ice. There is also some indication that the wintertime coverage of multiyear ice area in the Beaufort Sea foreshadows the severity of the subsequent summer ice season (Walsh and Zwally, 1990).

In seasonal sea ice zones, the distribution of new, young, and first–year sea ice types derived from the thin ice algorithm presented in section 3.1.4.2 was validated for the Bering Sea through a comparison with analyzed AVHRR imagery (Cavalieri, 1994). The results of this validation indicated that the SSMI and AVHRR ice type maps agreed in 80% of the cases on average with 99% confidence that the agreement does not arise by chance (Cavalieri, 1994). Further validation studies are required in other Arctic SSIZs.

Sea Ice Surface Classes

The classification of polar surfaces based on the clustering of brightness temperatures (or emissivities) in a multidimensional parameter space has been shown to provide a coherent representation of the ice cover from growth period to mid winter period. The outer zone is usually represented by three clusters that correspond to three stages in the development of ice in the

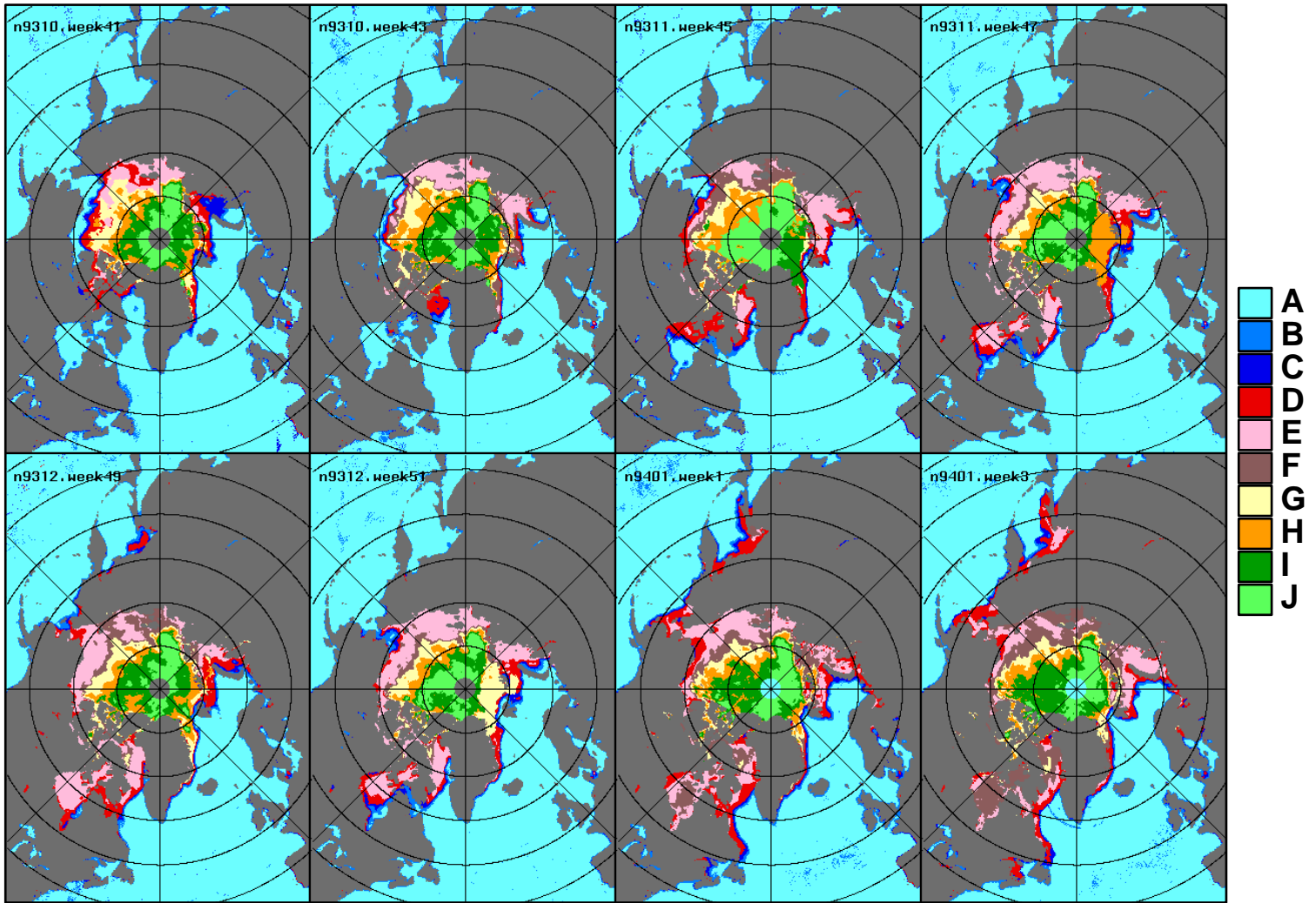**Arctic Weekly Ice Classes: Oct. 1993 – Jan. 1994**

Figure 16. Weekly ice cluster maps showing the location of clusters A through J (see text) in the Arctic region from October 1993 through January 1994. The week number is based on having 52 weeks a year.

marginal ice zone (e.g., from grease ice to pancake ice to young ice, or thicker pancake ice). Beyond the outer zone are first year ice which may be deformed or undeformed and may have snow cover of different thicknesses, granularities, and/or layering history. Two classes of first year ice are identified based on the two most dominant types of surfaces in the region. Also, three classes are identified in the perennial ice region. One corresponds to second year ice which has been observed to have emissivities different from those of older multiyear ice types. The second one may be relatively undeformed third and fourth year ice types, while the third may correspond to very old and highly deformed multiyear ice types.

The time series shown in Figure 16 provides a means to observe the validity of the classifications in most of the seasonal regions. The stability of the classification in the perennial ice region during winter also indicates that radiometrically different surfaces features are identified. The higher resolution and wider frequency range of the AMSR, compared to those of SSMI, will improve ability to discriminate the different surfaces. However, further validation, some of which is currently in progress (e.g., Massom et al., 1996), is required to establish accuracy. The statistical error (random component) in the estimate of the area of most of the ice classes is

about 2%. The systematic error is expected to be greater but is difficult to establish before AMSR data are available.

3.4 Practical Considerations

3.4.1 Numerical Computation Considerations

Both the NASA Team and Bootstrap algorithms have been run without problems at the National Snow and Ice Data Center DAAC for routine processing. The NASA Team algorithm has also been run at the Marshall DAAC for processing the SSMI Pathfinder Data Set. Given this history, we do not anticipate any computational problems with the AMSR hybrid sea ice algorithm. Each of the two basic algorithms are currently running on PCs and SGI workstations at Goddard; the AMSR hybrid sea ice algorithm will also be run on these PCs and workstations. Even daily Level 3 products will not pose a problem. An estimate to process one month of SSMI Level 3 data is of the order of 5 minutes on an SGI workstation. We do not anticipate computational problems for any of the special products either, although the computational time may be somewhat greater. All special products are currently produced on SGI workstations.

3.4.2 Programming/Procedural Considerations

Input to the hybrid AMSR sea ice algorithm will consist of Level 1C AMSR brightness temperatures, latitude, longitude, time and a land/ocean flag. The standard output sea ice products will consist of sea ice concentration, sea ice temperature and snow depth and will include latitude, longitude, and a time stamp. The computer code and documentation will be delivered to EOSDIS according to their guidelines. The algorithms will be coded in C and Fortran.

3.4.3 Quality Control and Diagnostics

Quality control of brightness temperatures will be done during the generation of the Level 1C products. The first step in the quality control of the sea ice products will consist of checking whether or not the retrieved sea ice products fall within reasonable limits. Diagnostics will be based in part on satellite sea ice climatology developed since the launch of the Nimbus 7 SMMR in 1978. These data will provide a useful measure of the seasonal and regional values for sea ice concentration and to some extent sea ice temperature. Quality control of snow depth will be more difficult, because very little data exists on the spatial scale of AMSR footprints.

3.4.4 Exception Handling

Exception handling will consist of flagging missing data and land. Missing brightness temperatures will result in setting a missing flag for the sea ice retrieval. The sea ice algorithm will not be run over land. It is presumed that out−of−range brightness temperatures will be handled in the generation of Level 1C products. Out−of−range retrievals will be handled within the algorithm. Diagnostics for checking out−of−range data will be used in the algorithms to determine whether the output should be flagged as unreasonable. In some cases, for example, sea ice concentrations greater than 100% (within 3σ) will be set to 100% (within 3σ) and sea ice concentrations less than 0 will be set to zero. Much larger discrepancies will be flagged as unreasonable.

4.0 Validation Program

The objectives of the validation program are: (1) to obtain a quantitative measure of the

accuracy of the AMSR−derived sea ice products; (2) to define problem areas or areas that need improvements; and (3) to provide a means to evaluate how well each of the sea ice products (both standard and special) meets the observational requirements specified by the EOS Science Plan (1997). Three standard and three special products will be generated. Validation is important because most of these products will be relatively new. The main emphasis will be the validation of the hybrid sea ice concentration standard product not only because of its relevance to the MTPE, as indicated earlier, but also because success in deriving the other two standard products depends on the accuracy of this parameter.

The initial phase which is currently being implemented is to take advantage of existing historical data. Field experiments in both Arctic and Antarctic regions have been undertaken since the launch of the Nimbus−7 SMMR. We will take advantage of data from these programs to validate, whenever possible, results from the final version of the algorithms. Historical high resolution satellite data (Landsat, Spot, Mos, etc.) will be used to extrapolate values from point measurements. Historical passive microwave data (SMMR, SSMI) and also TMI, and Adeos−2 AMSR will be used to test the algorithms. Furthermore, radiative transfer modeling results will be used to improve our understanding of the physics of the emission from sea ice and the effect of the intervening atmosphere. Such information is needed to assess limits in the accuracy of some of the products. It is highly desirable that both pre− and post−launch aircraft missions be conducted. A suite of microwave radiometers that measure radiances at frequencies and polarizations close to those planned for AMSR will be useful. An example of such system is the NASDA built Airborne Microwave Radiometer (AMR). An aircraft AMSR simulator will be complemented by an infrared system to measure surface temperature, the polarimetric SAR to help discriminate surface types, especially in the perennial ice regions, and a digital camera to evaluate surface properties and overall characteristics of the ice cover. The specific areas and times covered would include those where and when the PR−GR and the temperature corrected Bootstrap algorithms have significant differences. In addition, data is needed to improve ice−weather discrimination at the ice edge and in marginal ice zones. Such missions will be coordinated with validation programs for other AMSR parameters. The timing of the aircraft underflights will also be done to enable accurate comparative analysis with data from SSMI, TRMM TMI and ADEOS−2 AMSR instruments.

A NASA sea ice validation program for the DMSP SSM/I was completed in 1991 and may be used as a guide for the sea ice data validation plan for the AMSR (Cavalieri, 1992; Cavalieri, 1991; Cavalieri et al., 1991; Steffen and Schweiger, 1991). Other validation programs include a near simultaneous aircraft, submarine, and ship experiment over the Arctic (Comiso et al., 1991; Wadhams et al., 1992) and several cruises in the Antarctic (Comiso et al., 1989; Grenfell et al., 1994). Many major compaigns in the Arctic regions have also been undertaken (e.g., MIZEX east and west). Results from sea ice validation studies since the launch of the Nimbus 7 SMMR has been summarized (Cavalieri, 1992). We will take advantage of experiences from these programs to optimize the likelihood of success in the new validation missions. Data from the aircraft missions will be supplemented by data from Landsat, which has become a NASA system again and will be less expensive, and other high resolution satellite systems. The Landsat data and other systems will enable extrapolation of data obtained from the aircraft tracks to much wider area. The launch of the 40 channel MODIS system aboard EOS−AM will also open an oportunity to investigate new information about the ice cover that can be derived from such a system. Since MODIS will also be available aboard EOS−PM, the data will be used synergistically with AMSR data to optimize the accuracy of products derived from the latter. The

uses of Radarsat (and other satellite SAR data) and NSCAT (and other scatterometers) data for ice applications have not been well established but SAR is expected to be provide some critical information needed to verify ice type discrimination results while SAR, NSCAT, and MODIS will be useful for surface type classification.

A list of standard and special products and a summary of data to be used to validate each of them is given in Table 3. The list provides examples of systems that would be most suitable for validating the different parameters.

TABLE 3. Validation data sets for the proposed AMSR sea ice products.

Sea Ice Product	Validation Data
Standard	
Sea Ice Extent and Concentration	ADEOS – II Gobal Imager (GLI) LANDSAT MSS & TM; NOAA AVHRR RADARSAT; MODIS; Aircraft underflights
Sea Ice Temperature	ADEOS – II GLI; EOS–AM MODIS; AVHRR; Climatology; Buoys; Field and ice station data, Aircraft underflights
Snow Depth on Sea Ice	In–situ snow depth measurements Remotely sensed snow depth from aircraft.
Special	
Ice Displacement Vectors	Buoys, NSCAT, AVHRR
Sea Ice Type	ADEOS – II GLI; LANDSAT MSS & NOAA AVHRR; RADARSAT; MODIS; Aircraft underflights
Surface Classes	ADEOS – II GLI; LANDSAT MSS & NOAA AVHRR; RADARSAT; MODIS; Aircraft underflights

5.0 References

Badgley, F. I., Heat budget at the surface of the Arctic Ocean, in Proc. of the Symp. on the Arctic Heat Budget and Atmospheric Circulation, J. O. Fletcher, ed., pp. 267–277, 1966.

Ball, J. and X. Hall, A clustering technique for summarizing multivariate data, Behavioral Science, 12, 153–155, 1967.

Bryan, K., S. Manabe, and R. C. Pacanowski, A global ocean–atmosphere climate model. Part II. The ocean circulation, J. Phys. Oceanography 5, 30–46, 1975.

Budyko, M.I., Polar ice and climate, In Proceedings of the Symposium of the Arctic Hea Budget and Atmospheric Circulation, ed. by J.O. fletcher (ed), RM5233–NSF, Rand Corporation, Santa Monica, CA, 3–21, 1966.

Businger, S., and R. J. Reed, Polar lows, in Polar and Arctic Lows, Twitchell, P. F., E. A. Rasmussen, and K. L. Davidson, eds., A. Deepak, Hampton, VA, pp. 3–45, 1989.

Carleton, A. M., Satellite climatological aspects of the "polar low" and "instant occlusion," Tellus 37A, 433–450, 1985.

Cavalieri, D. J., NASA Sea Ice Validation Program for the Defense Meteorological Satellite Program Special Sensor Microwave Imager, J. Geophys. Res., 96, 21,969–21,970, 1991.

Cavalieri, D. J., The Validation of Geophysical Products Using Multisensor Data, Chapter 11, Microwave Remote Sensing of Sea Ice, (ed. by Frank Carsey), American Geophysical Union, Washington, D.C., 243–259, 1992.

Cavalieri, D. J., P. Gloersen, and T. T. Wilheit, Aircraft and satellite passive–microwave observations of the Bering Sea ice cover during MIZEX West, IEEETrans. Geoscience and Remote Sensing GE–24, 368–377, 1986.

Cavalieri, D. J., J. Crawford, M. Drinkwater, W. J. Emery, D. T. Eppler, L. D. Farmer, M. Goodberlet, R. Jentz, A. Milman, C. Swift, C. Wackerman, and R. L. Weaver, NASA sea ice validation program for the DMSP SSM/I: Final report, NASA TM 104559, pp. 126, 1992.

Cavalieri, D., A passive microwave technique for mapping new and young sea ice in seasonal sea ice zones, J. Geophys. Res., 99(C6), 12561–12572, 1994.

Cavalieri, D. J., P. Gloersen, and W. J. Campbell, Determination of sea ice parameters with the Nimbus 7 SMMR, J. Geophys. Res., 89, 5355–5369, 1984.

Cavalieri, D. J., K. M. St. Germain, and C. T. Swift, Reduction of weather effects in the calculation of sea ice concen– tration with the DMSP SSM/I, J.Glaciology, 41(139), 455–464, 1995.

Cavalieri, D. J., J. P. Crawford, M. R. Drinkwater, D. T. Eppler, L. D. Farmer, R. R. Jentz, C. C. Wackerman, Aircraft active and passive microwave validations of sea ice concentration from the DMSP SSM/I, J. Geophys. Res., 96, 21989–22008, 1991.

Chang, T. C., P. Gloersen, T. Schmugge, T. T. Wilheit, and H. J. Zwally, Microwave emission from snow and glacier ice, J. Glaciol. 16, 23–39, 1976.

Chang, A. T. C., J. L. Foster, and D. K. Hall, Nimbus 7 SMMR derived global snowcover parameters, Ann. Glaciol., 9, 39–44, 1987.

Colony R., and A. Thorndike, Sea ice motion as a drunkard's walk, J. Geophys. Res., 90, 965–974, 1985.

Comiso, J. C., Sea ice effective microwave emissivities from satellite passive microwave and infrared observations, J. Geophys. Res., 88, 7686–7704, 1983.

Comiso, J. C., Characteristics of Arctic Winter Sea Ice from Satellite Multispectral Micrwave Observations, J. Geophys. Res., 91, 975–994, 1986.

Comiso, J.C., Arctic Multiyear ice Classification and Summer Ice Cover using Passive Microwave Satellite Data, J. Geophys. Res., 95, 13411–13422, 1990.

Comiso, J.C., SSM/I ice concentrations using the Bootstrap Algorithm, NASA RP 1380, 50pp, 1995.

Comiso, J.C., Sea ice geophysical parameters in the Arctic and the Sea of Okhotsk using multichannel passive microwave data, Journal of Japanese Remote Sensing, 16(2), 32–46, 1996.

Comiso, J.C., D. J. Cavalieri, C. L. Parkinson, and P. Gloersen, Passive microwave algorithms for sea ice concentrations, Remote Sensing of the Env. (In Press, 1997).

Comiso, J.C., and R. Kwok, The summer Arctic sea ice cover from satellite observations, J. Geophys. Res.,101(C2), 28397–28416, 1996.

Comiso, J. C. and C. W. Sullivan, Satellite Microwave and In–Situ Observations of the Weddell Sea Ice Cover and its Marginal Ice Zone, J. Geophys. Res., 91(C8), 9663–9681, 1986.

Comiso, J. C., and H. J. Zwally, Antarctic Sea Ice Concentrations Inferred from Nimbus–5 ESMR and LANDSAT imagery, J. Geophys. Res., 87(C8), 5836–5844, 1982.

Comiso, J. C., S. F. Ackley, and A. L. Gordon, Antarctic Sea Ice Microwave Signature and their Correlation with In–Situ Ice Observations, J. Geophys. Res. 89(C1):662–672, 1984.

Comiso, J. C., T. C. Grenfell, D. Bell, M. A. Lange, and S. F. Ackley, Passive Microwave In Situ Observations of Winter Weddell Sea Ice, J. Geophy. Res., 94(C8), 10891–10905, 1989.

Comiso, J. C., P. Wadhams, W. Krabill, R. Swift, J. Crawford, and W. Tucker III, Top/Bottom multisensor remote sensing of Arctic sea ice, J. Geophy. Res., 96(C2), 2693–2711, 1991.

EOS Science Plan, in preparation, 1997.

Gloersen, P., and D. J. Cavalieri, Reduction of weather   effects in the calculation of sea ice concentration from   microwave radiances, J. Geophys. Res., 91(C3), 3913–3919, 1986.

Gloersen, P. and W. J. Campbell, Satellite and aircraft passive–microwave observations during the Marginal Ice Zone Experiment in 1984, J. Geophys. Res. 93, 6837–6846, 1988.

Gloersen P., W. J. Campbell, D. J. Cavalieri, J. C. Comiso, C. L. Parkinson, H. J. Zwally, (1992), Arctic and Antarctic Sea Ice, 1978–1987: Satellite Passive Microwave Observations and Analysis, NASA Spec. Publ. 511, 1992.

Gloersen, P., E. Mollo–Christensen, and P. Hubanks, Observations of Arctic polar lows with the Nimbus 7 Scanning Multichannel Microwave Radiometer, in Polar and Arctic Lows, P. F. Twitchell, E. A. Rasmussen, and K. L. Davidson, eds., A. Deepak, Hampton, Virginia, pp. 359–371, 1989.

Gloersen, P., T. C. Chang, T. T. Wilheit, and W. J. Campbell, Polar sea ice observations by means of microwave radiometry, in Advanced Concepts and Techniques in the Study of Snow and Ice, H. S. Santeford and J. L. Smith, eds., Nat. Acad. Sci, pp. 541–550, 1974.

Gordon, A., Deep Antarctic convection west of Maud Rise, J. Phys. Oceanography., 8, 600–612, 1978.

Grenfell, T. C., A theoretical model of the optical properties of sea ice in the visible and near infrared, J. Geophys. Res., 88, 9723–9735, 1983.

Grenfell, T. C., Surface–based passive microwave observations of sea ice in the Bering and Greenland Seas, IEEE Trans. Geoscience and Remote Sensing GE–24,378–382, 1986.

Grenfell, T. C., and J. C. Comiso, Multifrequency passive– microwave observations of first–year sea ice grown in a tank, IEEE Trans. Geoscience and Remote Sensing, GE–24, 826–831, 1986.

Grenfell, T. C., J. C. Comiso, M. A. Lange, H. Eicken, and M. R. Wenshahan, Passive microwave observations of the Weddell Sea during austral winter and early spring, J. Geophys, Res., 99(C5), 9995–10010, 1994.

Honda, M., K. Yamazaki, Y. Tachibana, and K. Takeuchi, Influence of Okhhotsk sea–ice extent on atmospheric circulation, Geophysical Research Letters, in press, 1996.

Josberger, E. G., P. Gloersen, A. Chang, and A. Rango, The effects of snowpack grain size on satellite passive microwave observations from the Upper Colorado River Basin, J. Geophys. Res., 101, 6679–6688, 1996.

Kan, E. P., The JSC clustering program ISOCLS and its applications matching processing of remotely sensed data, Symposium Proceedings, Lab. for Applications of Remote Sensing, Purdue University, October 16–18, 1973.

Killworth, P. D., Deep convection in the world ocean, Rev. Geophys. and Space Phys. 21, 1–26, 1983.

Kunzi, K. F., S. Patil, and H. Rott, Snow–cover parameters retrieved from Nimbus 7 Scanning Multichannel Microwave Radiometer data, IEEE Trans. Geoscience and Remote Sensing, GE–20, 452–467, 1982.

Liu, A. K., C. Y. Peng, B. Chapron, and E. Mollo–Christensen, and N. E. Huang, Direction and magnitude of wind stress over wave groups observed during SWADE, The Global Atmosphere–Ocean System, 3, 175–194, 1995.

Liu, A. K., D. J. Cavalieri, and C. Y. Peng, Sea ice drift from wavelet analysis of DMSP SSM/I Data, submitted, Int. J. Rem. Sens., 1996.

Lohanick, A. L., Microwave brightness temperatures of laboratory–grown undeformed first–year ice with an evolving snow cover, J. Geophys. Res., 98, 4667–4674, 1993.

Manabe, S. and R. J. Stouffer, Multiple–century response of a coupled ocean–atmosphere model to an increase of atmospheric carbon dioxide, J. Climate, 7(1), 5–23, 1994.

Markus, T. and D. J. Cavalieri, Snow depth distribution over sea ice in the Southern Ocean from satellite passive microwave data, submitted to AGU ARS (edited by M. Jeffries), 1997.

Maslanik, J. A., Effects of weather on the retrieval of sea ice concentration and ice type from passive microwave data, Int. J. Rem. Sens., 13, 34–57, 1992.

Massom, R. and J. C. Comiso, The classification of Arctic sea ice types and the determination of surface temperature using advanced very high resolution radiometer data, J. Geophys. Res., 99, 5201–5218, 1994.

Massom, R. A., M. R. Drinkwater, C. Haas, Winter snowcover on sea ice in the Weddell Sea, J. Geophys. Res., submitted, 1996.

Matzler, C., R. O. Ramseier, and E. Svendsen, Polarization effects in sea ice signatures, IEEE J. Oceanic Engineering, OE–9, 333–338, 1984.

Maykut, G. A., Energy exchange over young ice in the central Arctic, J. Geophys. Res., 83(C7), 3646–3658, 1978.

Parkinson, C. L., J. C. Comiso, H. J. Zwally, D. J. Cavalieri, P. Gloersen, and W. J. Campbell (1987), Arctic Sea Ice 1973– 1976 from Satellite Passive Microwave Observations, NASA Spec. Publ. 489, pp.296, 1987.

Peng, C. Y., A. K. Liu, B. Chapron, and E. Mollo–Christensen, Wavelet analysis of sea surface flux and wave modulation by swell, The Global Atmosphere–Ocean System, 3, 195–208, 1995.

Preller, R. H., J. E. Walsh, and J. A. Maslanik, The use of satellite observations in ice cover simulations, Chapter 22, in Microwave Remoate Sensing of Sea Ice, F. D. Carsey (ed.), Geophysical Monograph 68, American Geophysical Union, Washington, DC, 1992

Rothrock, D. A., D. R. Thomas, A. S. Thorndike, Principal Component Analysis of satellite passive microwave data over sea ice, J. Geophys. Res., 93: 2321–2332, 1988.

Schluessel, P. and H. Grassl, SST in polynyas: A case study, International Journal of Remote Sensing, 11(6), pp.933–945, 1990.

Steffen, K. and A. Schweiger, NASA team algorithm for sea ice concentration retrieval from the Defense Meteorological Satellite Program Special SensorMicrowave Imager: Comparison with Landsat Imagery, J. Geophys. Res., 96(12), 21971–21987, 1991.

Stommel, H., On the smallness of sinking regions in the ocean, Proc. Nat. Acad. Sc., USA 48, 766–772, 1962.

Svendsen, E., K. Kloster, K., B. Farrelly, O. M. Johannessen, J. A. Johannessen, W. J. Campbell, P. Gloersen, D. J. Cavalieri, and C. Matzler, Norwegian Remote Sensing Experiment: Evaluation of the Nimbus 7 Scanning multichannel microwave radiometer for sea ice research, J. Geophys. Res., 88, 2781–2792, 1983.

Sturm, M., K. Morris, and R. Massom, The character and distribution of the winter snow cover on the sea ice of the Bellingshausen, Amundsen and Ross Seas, Antarctica, 1994–1995, submitted to AGU Antarvctic Research Monographs, 1997.

Swift, C. T., L. S. Fedor, and R. O. Ramseier, An algorithm to measure sea ice concentration with microwave radiometers, J. Geophys. Res., 90, 1087–1099, 1985.

Vowinckel, E., and S. Orvig, The climate in the north polar basin, in Climate of the Polar Regions, Vol.14 of World Survey of Climatology, Elsevier, Amsterdam, pp. 129–252, 1970.

Wadhams, P., W. Tucker, W. Krabill, R. Swift, J. Comiso, and N. Davis, The relationship between sea ice freeboard and draft in the Arctic Basin, and implications for ice thickness monitoring, J. Geophys. Res., 97(C12), 20325–20334, 1992.

Walsh, J. E., and H. J. Zwally, Multiyear sea ice in the Arctic: model– and satellite–derived, J. Geophys. Res. 95, 11,613–11,628, 1990.

Wensnahan, M., Maykut, G. A., Grenfell, T. C., and D. P. Winebrenner, Passive microwave remote sensing of thin sea ice using principal component analysis, J. Geophys. Res., 98, 12,453–12,468, 1993.

Wharton, S.W. and Y.C. Lu, The land analysis system: A general purpose system for multispectral image processing, Prodeedings of IGARSS87 Symposium, Ann Arbor, Michigan, 18–21, 1987.

Worby, A. P., and R. A. Massom, The structure and properties of sea ice and snow cover in East Antarctic pack ice, Antarctic CRC, Research report, 7, 191 pp., 1995.

Zwally, H. J., J. C. Comiso, C. L. Parkinson, W. J. Campbell, F. D. Carsey, F.D., and P. Gloersen, Antarctic sea ice, 1973–1976: satellite passive microwave observations, NASA SP–459, 1983.